Trends in Applied Spectroscopy
Vol. 8, 2010

Review

# Surface photovoltage spectroscopy – an advanced method for characterization of semiconductor nanostructures

**V. Donchev*, Ts. Ivanov, K. Germanova, and K. Kirilov**
Faculty of Physics, Sofia University, 5, blvd. J. Bourchier, Sofia-1164, Bulgaria

**TABLE OF CONTENTS**



**ABSTRACT**

In this review we describe some new approaches in the surface photovoltage spectroscopy (SPS) performed in the metal-insulator-semiconductor operation mode, which are related to open questions in the SPS characterization of nanostructures. The first new approach is based on surface photovoltage (SPV) phase spectroscopy. We show that i) the sign of the bandgap-related knee in the spectrum

*Corresponding author
vtd@phys.uni-sofia.bg

of the SPV phase modulus is positive (negative) for downward (upward) surface band bending and ii) for the case of non-linear recombination, the SPV phase spectrum reflects the features of the optical absorption coefficient spectrum. We demonstrate the necessity of simultaneous examination of both amplitude and phase SPV spectra in order to understand correctly the experimental data. As a second original approach, we have developed a vector model, in which the SPV signal is represented by a radial vector, containing all the information given by the amplitude and phase SPV spectra. Further, after a brief overview of the SPS characterization of nanostructures in the last decade, we present the results of our pioneering SPS studies of various nanostructures with graded interfaces including AlAs/GaAs superlattices with GaAs embedded quantum wells, multilayer InAs/InP quantum wires, InAs/InGaAlAs quantum dashes-in-well laser structures and multilayer InP/GaAs type II quantum dots. The interpretation of the amplitude and phase SPV spectra is carried our by the proposed vector model for the SPV signal in parallel with the analysis of data obtained by other experimental methods and electronic structure calculations. As a result valuable information about the investigated systems is obtained.

**KEYWORDS:** surface photovoltage, SPV phase spectroscopy, embedded quantum wells, quantum wires, quantum dashes, type II quantum dots

**ABBREVIATIONS**

AFM - atomic force microscopy
CB - conduction band
CPD - contact potential difference
DWELL - dash-in-well
EFA - envelope function approximation
EQW - embedded quantum well
ETB - empirical tight binding
IFVD - impurity free vacancy disordering
ITO - indium-tin-oxide
MIS - metal-insulator-semiconductor
ML - monolayers
NIID - nitrogen ion-implantation induced disordering
PL - photoluminescence
QD - quantum dot
QDH - quantum dash
QW - quantum well
QWR - quantum wire
SCH - separate confinement heterostructure
SCR - space charge region
SI - semi-insulating
SL - superlattice
SPS - surface photovoltage spectroscopy
SPV - surface photovoltage
VB - valence band
WL - wetting layer

## 1. INTRODUCTION

The surface photovoltage spectroscopy (SPS) is a powerful non-destructive and contactless characterization method, which has been successfully applied for characterization of different semiconductor bulk materials and nanostructures [1-3]. It is a highly sensitive technique, which can give important information about the electronic structure and optical properties of nanostructures even at room temperature. Due to its versatility the SPS in many cases successfully competes with other spectroscopic methods, such as optical absorption (transmission), photoluminescence (PL), photoluminescence excitation, electroreflectance spectroscopy, etc. The SPS is based on the measuring and analysis of the spectral dependence of the surface photovoltage (SPV) phenomenon. The basic principles and applications of the SPS are discussed in the review papers [1, 2] and in Sec. 2 of this article. The SPV measurements are performed mainly by means of Kelvin probe or metal-insulator-semiconductor (MIS) structure operation modes [1] (see also Sec. 3 of this paper). Due to some advantages [1], the MIS mode has gained popularity and is widely used in recent years [4-6]. Nevertheless, there are still open questions in this field, concerning the development of the data analyses and the application to study advanced complicated nanostructures.

In this review paper we describe some new aspects of the SPS, which are a subject of study in our pioneering works, devoted to the above mentioned open questions [7-14].

Most of the SPS investigations have been devoted to the measurement and analysis of the SPV

amplitude spectra [15-19]. However the spectral dependence of the SPV phase also may give essential information about the processes which contribute to the SPV signal generation in the sample. Nevertheless there are few studies concerning this interesting problem. For example, the works [15-18, 20-25] devoted to SPV characterization of nanostructures study only SPV amplitude spectra and do not present results about the SPV phase behavior.

In our work [10] we have proposed a new approach for characterization of semiconductor nanostructures and bulk materials based on measurements of SPV phase spectra in MIS operation mode under modulated illumination. In this connection we have demonstrated the necessity of simultaneous examination of both SPV amplitude and SPV phase spectra in order to obtain correct understanding of the experimental data.

As another original approach, we have developed a vector model for representation of the SPV signal in order to achieve an easier and reliable analysis of the SPV amplitude and phase spectra [9].

A variety of SPS applications for characterization of single (or multi-) quantum wells (QWs) and regular superlattices (SLs) have been discussed in the literature and are briefly reviewed in Sec. 6.1.1. of this article.

In the last time special interest is devoted to relatively new nanostructures, which represent short-period AlAs/GaAs SLs with GaAs embedded quantum wells (EQWs). These structures show a number of new physical properties often different from those of single QWs and unperturbed SLs, resulting from the interaction between their components. To our knowledge the first SPS studies of such structures were performed in our works [7-10], the main results of which are described in Sec. 6.2.

Currently, simultaneously with the QWs and SLs, increasing interest attract nanostructures with lower dimension – quantum wires (QWRs), nanorods and quantum dots (QDs), and new complicated combinations of them. They allow fabrication of optoelectronic and photonic devices with superior operation parameters, e.g. larger optical gain, lower threshold current and weaker temperature dependence of the laser and light-emitting diode spectra. SPS investigations of different nanostructures containing QDs and nanorods are briefly reviewed in Secs. 6.1.2. and 6.1.3., respectively. No reports were found for SPS of QWRs.

In the last years increasing efforts are dedicated to the fabrication and study of multilayer structures including InAs/InP QWRs [26, 27], since they are promising candidates for emitters in the range 1.30-1.55μm, suitable for the optical fiber telecommunication systems. The same reasons justify the development of more complicated structures, including InAs quantum dashes (QDHs) [28], often embedded in QWs [29, 30]. Concerning the QDs, most of the studies are devoted to the InAs/GaAs system with type I heterointerfaces [31, 32]. Few works deal with InP/GaAs QDs [33, 34], although their type II interfaces make them suitable for optical memory devices.

To our knowledge the first SPS studies of multilayer InAs/InP QWRs, InAs/InGaAlAs QDHs and InP/GaAs QDs were performed in our pioneering works [11-14], the main results of which are described in Secs. 6.3., 6.4. and 6.5., respectively.

It is to be noted that our SPS experimental results are discussed and explained employing the new approaches depicted above, namely the simultaneous analysis of the amplitude and phase SPV spectra and the vector model for the SPV signal. The SPS results are compared with those obtained by PL spectroscopy and by electronic structure calculations in frames of the envelope function approximation (EFA) and the empirical tight binding (ETB) methods where a very good agreement is found. As a result valuable information about the optical properties, the electronic structure and the interface grading effect in the investigated systems has been obtained.

## 2. Basic principles

The purpose of this section is to present a brief introduction to the basic principles of the SPS as well as to give the essential definitions, concepts

and equations, which are necessary for the understanding of the following sections. In the description below we follow the excellent reviews of Kronik and Shapira [1] and the book by Many *et al.* [35], where a more detailed discussion can be found.

The SPS is based on the measurement and analysis of the spectral dependence of the SPV phenomenon. The latter consists in the change of the surface potential, induced by optical generation of free carriers, followed by their space redistribution in the sample. So, the SPV, denoted by $\delta V_s$, is expressed as the difference between the surface potential value under illumination $V_s^*$ and that in dark $V_s$, i.e.:

$$\delta V_s = V_s^* - V_s. \quad (1)$$

Let us consider the SPV induced at the free surface of a semiconductor sample with grounded back Ohmic contact. If no external field exists, the charge conservation law, $Q_t + Q_{ss} = 0$ [$Q_t$ – the charge in the surface states, $Q_{ss}$ – the charge in the space charge region (SCR)] is valid in dark as well as under illumination. In the last case the two charges may change separately in wide ranges, maintaining however the above depicted equation. The exciting light generates free carriers via band-to-band and/or trap-to-band transitions. Thus, due to the built-in field in the SCR a significant amount of charge may be exchanged between the surface and the bulk and/or redistributed within the surface or the bulk. Since the charge distribution and the electric potential are interdependent through the Poisson and the continuity equations, the potential distribution near the surface changes and hence the surface potential changes, too, i.e. a SPV arises.

Usually outside the SCR there is no electric force, which can redistribute the carriers and therefore the bulk remains quasi-neutral. An exception from this situation is the Dember effect, which consists in the formation of electric field in the bulk under illumination. This is due to the non-uniform generation of electrons and holes in the sample and their non-equal mobilities.

There are two basic mechanisms of the SPV formation depending on the relation between the incident light energy $h\nu$ and the semiconductor bandgap energy $E_g$. For $h\nu > E_g$ ($h\nu < E_g$) one utilizes the term super-bandgap (sub-bandgap) SPV. In this paper we shall consider mainly phenomena related to super-bandgap SPV. That is why the discussion of the sub-bandgap SPV is omitted here.

The dominant mechanism for generation of super-bandgap SPV is shown in Fig. 1(a) for the case of upward energy band bending at the surface with respect to the bulk. The built-in electric field in the SCR repels the electrons from and attracts the holes towards the surface. This reduces the electron density in the surface states and hence decreases the band bending. In the second mechanism, shown in Fig. 1(b) and (c), electrons [Fig. 1(b)] or holes [Fig. 1(c)] are preferentially trapped at surface states. This changes the surface charge and thus the surface potential. The second mechanism takes place usually in bulk samples, but only if the surface band bending in thermal equilibrium is small. It is more important in polycrystalline materials. The discussion given above concerns the free surface of the semiconductor, but by proper design and interpretation of the SPV experiment one can effectively gain information about various buried interfaces.

## 3. Experimental methods for SPV measurements

The SPV measurement is non-trivial, because the surface potential is a built-in potential and therefore, it cannot be measured simply with a voltmeter. Besides, in the case of a free surface, the application of any contact for indirect electrical measurements of the built-in voltage (e.g., in the current - voltage or the capacitance - voltage methods) will modify the surface properties and hence the physical quantity under study. This peculiarity of the surface potential has provoked the elaboration of many techniques for measuring its value or its changes without applying a direct electrical contact. In this section we give a brief description of the two basic techniques utilized to that purpose.

### 3.1. Kelvin probe technique

This technique is based on measuring the contact potential difference (CPD) between the sample and a closely positioned metal electrode, which

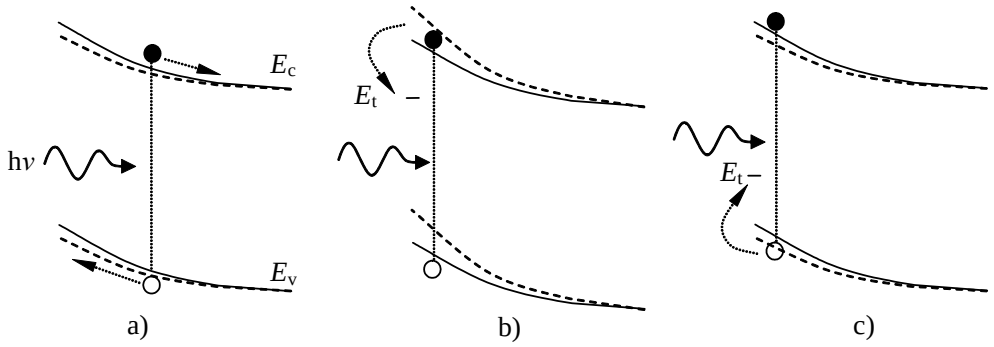


**Fig. 1.** SCR band diagram for n-type semiconductor with depleted surface for different SPV generation mechanisms in the case of super-bandgap illumination: a) carrier separation by the build-in electric field; b) preferential electron capture in surface states with energy $E_t$; c) preferential hole capture in surface states. The solid and dashed lines denote the band line-up before and after illumination respectively.

are short-circuited. The CPD $V_{CPD}$ is given by the difference between the work functions $W$ of the two materials: $eV_{CPD} = W_S - W_M$. An important point is that the metal work function does not depend on the illumination. Thus, the change of the CPD under steady light illumination with respect to dark gives the change of the work function of the sample, which is related to the change of the surface potential by the following equation:

$$e\delta V_{CPD} = \delta W_S = -e\delta V_s \quad (2)$$

The CPD between the sample and the metal electrode is measured by forming a parallel plate capacitor with them. When its two plates are short-circuited, charges flow from the material with lower $W$ towards that with higher $W$ until equilibration of the Fermi levels is achieved. The charge on the capacitor plates induces an electric field in the gap between them and a drop of the local vacuum level across this gap. Contrary to a standard capacitor, the potential drop here is built-in and is achieved under zero external bias. Therefore in order to measure $V_{CPD}$ in the modern Kelvin technique one employs a vibrating electrode and an external dc bias in series with the built-in field. The vibration is achieved by electromechanical or piezoelectric techniques, which provide a precise control of the electrode-to-sample distance. The resulting capacitance changes induce corresponding changes in the capacitor charge and hence an ac current in the external circuit. This current can be zero if and only if the capacitor is discharged, which is achieved when the external voltage is equal and opposite in sign to the $V_{CPD}$. Thus, $V_{CPD}$ is found easily, even automatically by determining the external dc bias, which nullifies the external ac current.

### 3.2. Metal-insulator-semiconductor operation mode

In this method the metal electrode is fixed and the plate capacitor is represented by a MIS structure. The MIS capacitor is charged and afterwards it is brought into open-circuit mode by disconnecting the two terminals. The illumination with chopped light induces alternative changes of the surface potential due to the SPV effect. This produces equal changes of the voltage between the two capacitor plates. In this way the ac SPV signal, obtained at the semiconductor-insulator interface can be obtained directly by measuring the photoinduced ac voltage between the MIS capacitor terminals.

The MIS operation mode is applicable also in studying free semiconductor surfaces by placing a static metallic grid in proximity to the sample, so that the air or the vacuum gap plays the role of insulator, as proposed firstly by Morrison [36]. In the latter other insulators that do not change the surface properties (e.g. mica) have been also employed [37].

Lately different implementations of the MIS operation mode are widely used. This is due to some advantages, which it has over the Kelvin probe mode, such as a lower noise level, superior

temporal resolution, easier scanning applications, possibility to replace the Ohmic back contact by contactless capacitive coupling, possibility for low-temperature measurements, etc [1].

The SPS in the MIS operation mode has been successfully used for characterization of semiconductor bulk materials, multilayers and nanostructures. Nevertheless, there are still open questions in this field, concerning the development of the measurement technique, the improvement of the data analysis and the extension of the application towards characterization of new complicated nanostructures.

## 4. Experimental set-up for SPS performed in MIS operation mode

In this section we present our experimental set-up for SPS, which is performed in MIS operation mode and allows fully automated measurements in a wide spectral and temperature range. It is schematically represented in Fig. 2. The sample is mounted on a grounded copper platform positioned in a continuous flow optical cryostat. Two types of semitransparent electrode (probes) are used. The first one is a gold grid stretched over a frame, isolated from the sample by an 8 μm polyimide sheet, which has an opening 3 mm in diameter used for illumination. The second one is $SnO_2$ film deposited on quartz glass. The probe holder is tightly fixed and insulated from ground. By means of an additional screw, the holder can be bent so that the probe presses the sample against the copper platform. The sample surface is illuminated through the probe by means of a 50 or 100W halogen tungsten lamp along with a 0.22 m SPEX grating monochromator, a filter to cut off the high-order diffraction and a PTI OC4000 optical chopper. The probe signal with respect to ground is fed to a high-impedance unity gain buffer (UGB) and then measured by an EG&G 5207 Lock-in amplifier. The shield and the core of the cable carrying the SPV signal from the probe to the UGB input are kept at the same potential in order to reduce the cable capacitance effect. To that purpose the cable shield is electrically connected to the UGB output.

Two methods for achieving constant photon flux density $\Phi$ incident on the sample at each wavelength are used. In the first one, the lamp voltage is precalibrated with a Golay detector (Oriel IR50), which has a flat response throughout the whole range of wavelengths used in the experiment. In the second method part of the light is reflected with a small mirror towards the same Golay detector through second optical chopper (11 Hz required for correct measurement) and the signal from the detector is fed to a second lock-in amplifier (Brookdeal 9530). This feedback is used to adjust the position of a neutral density filter with graded optical density, thus achieving a quasi-real-time control of the photon flux for each wavelength. By changing the monochromator slits

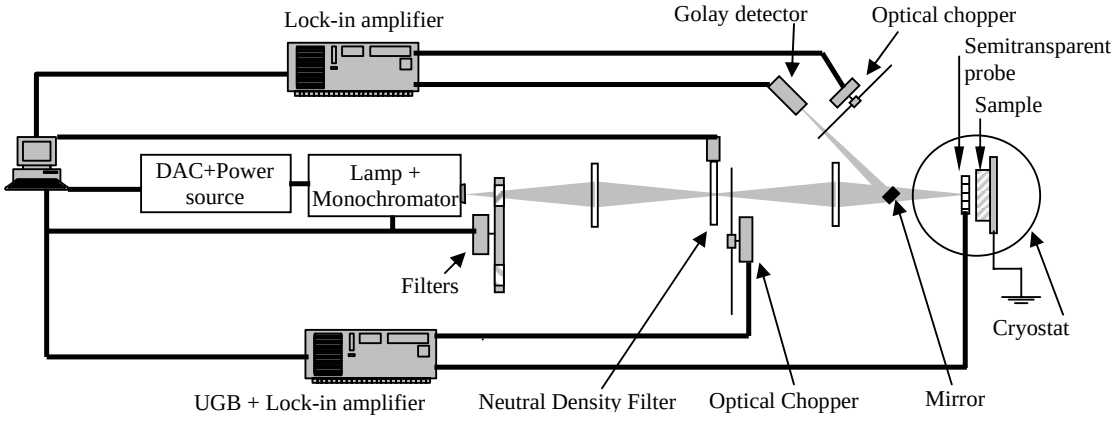


**Fig. 2.** Experimental set-up for SPV measurements in MIS mode. Reprinted with permission from [Ivanov, Ts., Donchev, V., Germanova, K., and Kirilov, K. J. Phys. D: App. Phys., 42, 135302, (2009)] Copyright IOP Publishing Ltd.

width and/or using neutral density filters, $\Phi$ is varied in the range $1\times10^{13}$ - $8\times10^{14}$ $cm^{-2}s^{-1}$. The uncertainties are ± 2% and ± 0.5%, respectively for the first and second method for achieving constant $\Phi$.

In order to study the SPV phase retardation with respect to the light modulation in a correct way it is necessary to take into account or eliminate the possible phase shifts between: i) the SPV and the voltage measured by the Lock-in amplifier; ii) the light modulation and the reference signal, which is generated by the optical chopper. In our experiment this has been realized as follows:

i) The sample back contact was disconnected from ground and an external voltage source was applied between this contact and the ground, keeping the MIS capacitor in dark. Thus, we replaced the photovoltage by the external voltage source, which was either a Wavetek function generator (impedance 50 Ω) or the Lock-in internal oscillator output (impedance 600 Ω) similarly to [38]. The external voltage source provided also the reference signal, necessary for the Lock-in. With both sources we obtained the same value for the voltage transfer factor (≈0.4 for the gold grid probe and almost 100% for $SnO_2$ probe) and practically zero phase shift between the external voltage and the measured signal.

ii) A fast (with respect to the light modulation frequency) photodiode positioned in the place of the sample was illuminated and its signal was monitored by the Lock-in. This signal was fed also to a two channels oscilloscope together with the reference signal from the chopper. In the general case, due to the arbitrary position of the light spot on the chopper wheel, a phase shift between the two signals is present, which can be observed on the oscilloscope and/or measured by the Lock-in. In our experiments this phase shift was compensated by means of the built-in phase shifter of the optical chopper.

The results described in i) and ii) enable us to define the zero value of the SPV phase measured in our experiment - it is the phase of the reference signal. Thus, any nonzero phase values observed in the experiment are attributed to processes taking place in the sample, which allows investigating their origin and kinetics [39-41].

The following measurements procedure is applied. The signal X, which is in phase with the reference signal (i.e. with the light modulation, as explained above) and the signal Y, shifted in phase by $90^o$, are measured and the obtained values are used to calculate the SPV amplitude $A$ and phase φ by the following formulae: $A = (X^2 + Y^2)^{1/2}$ and $\varphi = \text{arctg}\,(Y/X)$ . Taking into account the signs of X and Y and the periodicity of the arctg function we obtain φ between –180° and +180° or between 0° and 360°.

All the measurements are performed at room temperature with normal incident light, modulated with 94 Hz, except where explicitly stated other values. The scanning is from high toward low wavelength values.

## 5. Some new aspects of the SPS

### 5.1. SPV phase spectroscopy

In the SPS mainly the spectral dependence of the SPV amplitude is measured and analyzed [15-19]. However the spectral dependence of the SPV phase also carries important information about the SPV formation processes. Nevertheless, it has been a subject of relatively less studies. In particular, most of the papers devoted to SPV characterization of nanostructures have reported only SPV amplitude spectra and do not present results about the SPV phase behavior [15-18, 20-22, 24, 25].

Here we point out the necessity of simultaneous examination of both SPV amplitude and SPV phase spectra in order to obtain correct understanding of the experimental data. In this connection we present **two original approaches**, concerning the application of the SPV phase spectral measurements for characterization of bulk semiconductors and nanostructures.

#### 5.1.1. SPV phase and energy band bending

The **first original approach** concerns the information about the direction of the energy band bending, which can be retrieved from the SPV phase spectral measurements. The phase φ of the SPV signal, corresponding to a single SPV generation process, is related to the direction of the energy band bending at the place where the signal is generated. This idea is illustrated in Fig. 3.

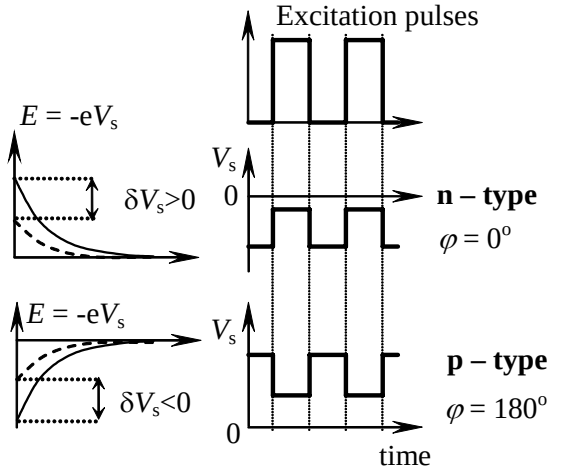


**Fig. 3.** Left: Surface band bending in dark (solid lines) and under illumination (dashed lines) of the conduction band edge in n-type (up) and p-type (down) semiconductors under depletion; Right: Surface potential as a function of time in the case of n-type and p-type semiconductor compared to the light excitation pulses in the ideal case where no phase retardation exists. Reprinted with permission from [Ivanov, Ts., Donchev, V., Germanova, K., and Kirilov. K. J. Phys. D: App. Phys., 42, 135302, (2009)] Copyright IOP Publishing Ltd.

The SPV value $\delta V_s$ is given by Eq. (1) in Sec. 2, where it is shown that $\delta V_s > 0$ ($\delta V_s < 0$) for upward (downward) energy band bending. In the ideal case of very fast carrier generation, redistribution and recombination processes, which do not introduce any phase retardation of the SPV signal, the SPV phase, measured with respect to the light excitation, would be zero for upward band bending ($\delta V_s > 0$) and $180^o$ for downward band bending ($\delta V_s < 0$). In the real case, due to the retardation of the signal with respect to the light excitation, the SPV phase is in the IV$^{th}$ quadrant for upward and in the II$^{nd}$ quadrant for downward band bending.

In this non-ideal case it is better to consider a SPV phase spectrum rather than the value of φ at a single photon energy $h\nu$. When scanning from low to high $h\nu$ the onset of the band-to-band optical transitions will give rise to a relatively fast SPV formation process with strong amplitude. As a result φ will shifts towards $\pm 0^o$ in the case of upward and towards $\pm 180^o$ in the case of downward band bending. In other words for upward (downward) band bending |φ| will decrease (increase) with increasing $h\nu$. This will result in a bandgap-related knee in the |φ| spectrum, which sign is negative (positive) for upward (downward) band bending.

The use of a SPV phase spectrum, rather than the value of φ at a single $h\nu$ is obligatory in the case where optical transitions with defect levels participation have a substantial contribution to the SPV signal under supper-bandgap excitation. Their contribution is superimposed on that of the band-to-band transitions and thus the resulting SPV phase could have various values depending on the concrete mechanisms involved in the SPV signal formation from the defect levels. However, the onset of the band-to-band transitions will change φ in the same way as depicted above and hence the sign of the bandgap-related knee in the |φ| spectrum will give again the direction of the energy band bending.

Most semiconductor surfaces are either depleted or inverted at equilibrium, which means that the surface band bending is upward (downward) for an *n*-type (*p*-type) semiconductor [1]. So, examining the sign of the bandgap-related knee in the |φ| spectrum one can determine the semiconductor type. A limitation of the proposed approach for determining the semiconductor type arises in the case of small surface band bending, where the Dember effect contribution dominates over the band-bending-related contribution to the measured SPV signal [1]. In this case, if the electrons diffuse faster then the holes (which is the most common situation), the SPV phase is in the IV$^{th}$ quadrant, as it is for an n-type semiconductor.

#### 5.1.2. SPV phase and optical absorption coefficient

Another important point is the spectral behaviour of the SPV phase, φ($h\nu$), which in fact reflects its dependence on the optical absorption coefficient α($h\nu$). The dependence of the SPV amplitude on α($h\nu$) has been discussed and modelled in various papers [1, 18, 42], but there are almost no similar studies for the SPV phase. The **second new approach** concerns the relation between φ($h\nu$) and α($h\nu$).

It is known that, in the case of quadratic recombination, increasing the generation rate α($h\nu$)$\Phi$

results in an increase of the excess carrier concentration $\Delta n(t)$ at a given moment $t$ and consequently of the recombination probability, which is proportional to $\Delta n^2$ [43]. This leads to a decrease of the momentary excess carrier lifetime $\tau(t)$, because it is inversely proportional to $\Delta n(t)$ [43]. Consequently, increasing $\alpha(h\nu)$ (or $\Phi$) will reduce the phase retardation of the $\Delta n(t)$ variations, measured with respect to the light modulation and this will reduce the SPV phase retardation, too, because $\delta V_s$ is a monotonous function of $\Delta n$. Similar relations should be expected also in the other cases of non-linear recombination, while for linear recombination $\tau$ is independent on time as well as on $\alpha(h\nu)\Phi$ [43]. So, in the non-linear recombination cases an increase (decrease) of $\alpha(h\nu)$ will result in a decrease (increase) of the SPV phase retardation, i.e. to anticlockwise (clockwise) change of $\varphi$.

It is worth noting that in the general case the dependence $\varphi(\alpha)$ is non-linear and complicated. As stated above it is realized through $\tau(t)$. So, we first analyze the relation between $\alpha(h\nu)$ and $\tau(t)$. In the case of quadratic recombination and rectangular light modulation this relation for the increasing (light on) and decreasing (light off) transients $\Delta n(t)$ is given by Eqs. (3) and (4), respectively [43]

$$\tau(t) = \frac{cth(t\sqrt{\gamma\beta\alpha\Phi})}{\sqrt{\gamma\beta\alpha\Phi}}, \tag{3}$$

$$\tau(t) = t + \frac{1}{\sqrt{\gamma\beta\alpha\Phi}} \tag{4}$$

where $\gamma$ is the recombination coefficient and $\beta$ - the quantum efficiency. It is seen that for a given moment $t$, the dependence of $\tau(t)$ on $\alpha(h\nu)$ is a decreasing non-linear function. The decrease is faster for low $\alpha(h\nu)$. Similar behaviour of $\tau(t)$ versus $\alpha(h\nu)$ should be expected also in the other cases of non-linear recombination. However, one should not forget that at low values of $\alpha(h\nu)\Phi$ the recombination regime becomes linear and $\tau = const$ should be used instead of Eqs. (3) and (4).

Further, we analyze qualitatively the relation between $\tau(t)$ and $\varphi$ in the case of quadratic recombination and rectangular symmetrical shape of the modulated light intensity. Fig. 4 represents normalized SPV signal transients during one period $T$ of the light modulation in the case of upward band bending. They correspond to different values of $\alpha$, i.e. to different values of $\tau(t)$, according Eqs. (3) and (4). In the ideal case of infinitely fast SPV formation processes the SPV transient follows the excitation light sequence (curve 1), which results in zero SPV phase retardation. In the real cases with $0 < \tau_2(t) < \tau_3(t)$ a displacement of the geometrical centre of the SPV transient toward subsequent time moments appears (curves 2 and 3, respectively) with respect to the ideal case (curve 1). This displacement, represented qualitatively by $\Delta t_2$ and $\Delta t_3$ in Fig. 4, corresponds to phase retardations $\Delta\varphi_2 = 2\pi\Delta t_2/T$ and $\Delta\varphi_3 = 2\pi\Delta t_3/T$ of the SPV signal with respect to the light excitation. The phase retardation is smaller for smaller $\tau(t)$ ($\Delta\varphi_2 < \Delta\varphi_3$). At very high $\alpha(h\nu)\Phi$ [very small $\tau(t)$] $\Delta t$ and $\Delta\varphi$ approach zero, and correspondingly $\varphi$ tends to its saturation point, which is close to -0 for upward and $\pi$ for

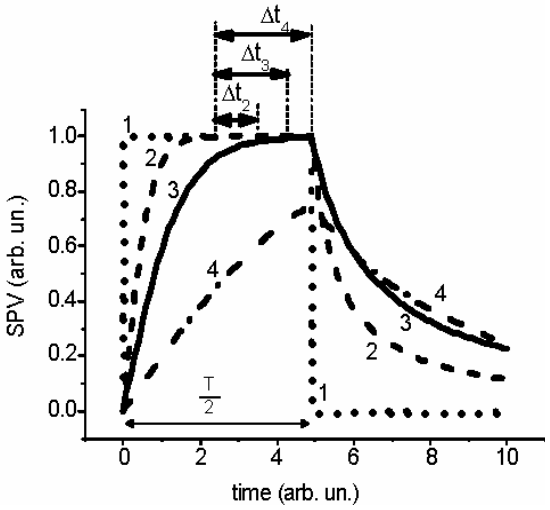


**Fig. 4.** Normalized SPV signal transients during one period $T$ of the light modulation, corresponding to different optical absorption coefficients for the case of non-linear recombination. Reprinted from [Donchev, V., Kirilov, K., Ivanov, Ts., and Germanova, K. Mat. Sci. & Engineering B, 129(1-3), 186-192. "Surface photovoltage phase spectroscopy – a handy tool for characterisation of bulk semiconductors and nanostructures"] Copyright (2006), with permission from Elsevier.

downward band bending, respectively. As a result the dependence $\varphi(\alpha)$ becomes weaker, i.e. $\varphi$ is less sensitive to the $\alpha(h\nu)$ changes. Similar behaviour of $\varphi$ with increasing $\alpha(h\nu)$ should be expected also in the other cases of non-linear recombination. On the other hand, at small $\alpha(h\nu)$ (or $\Phi$) the recombination becomes linear, $\tau$ = *const* and therefore $\varphi$ does not depend on $\alpha$.

The dependence $\varphi(\alpha)$ is influenced by the light modulation frequency *f*, because $\varphi$ depends also on *f* [39-41]. When *f* increases and approaches $\tau^{-1}(t)$, the SPV transient can not reach the stationary value. Such a situation is represented by curve 4 in Fig. 4, which corresponds to $\tau_4(t) > \tau_3(t)$ (and therefore $f \leq \tau_4^{-1}(t) < \tau_3^{-1}(t)$).

In this case $\Delta t_4$ is close to $T/4$ and therefore $\Delta\varphi_4$ tends to $\pi/2$. As a result the dependence $\varphi(\alpha)$ becomes weaker. $\varphi$ is less sensitive to the $\alpha(h\nu)$ changes also at $f << \tau^{-1}(t)$ [$T >> \tau(t)$], where $\Delta\varphi$, being proportional to $1/T$, tends to zero (see the previous paragraph). It is worth noting that the frequency dependence of $\Delta\varphi$ derived from Fig. 4 is in accordance with the results from [39-41].

One more mechanism can contribute to the decrease of the SPV phase retardation with increasing $\alpha(h\nu)$. For larger $\alpha(h\nu)$ the region from the sample, which absorbs the light, shrinks towards the surface and as a result carrier diffusion plays a minor role in the SPV signal formation as explained in [39, 40]. This effect is however expected at high frequencies, of the order of the inverse value of the carrier lifetime (tens of kHz in Si).

Summarizing Sec. 5.1., we can say that the SPV phase will be more sensitive to changes in the optical absorption coefficient for intermediate values of the carrier generation rate as well as of the light modulating frequency. Consequently, at such experimental conditions the SPV phase spectrum will better reveal small features in the $\alpha(h\nu)$ spectrum. It is important to note that these experimental conditions are commonly used in the SPV experiments.

### 5.2. Vector model for representing the SPV signal

The SPV signal is represented by its amplitude and phase and both their spectral dependences are recorded and give valuable information about the sample under study. This enables presentation of the SPV signal as a radial vector with the same magnitude as the SPV amplitude and angle with respect to the X-axis equal to the SPV phase (see Fig. 5). The SPV amplitude change leads to change of this vector's magnitude, while the SPV phase change is represented by vector rotation. According to the discussion presented in Sec. 5.1.1 the angle of the SPV vector, corresponding to a single SPV generation process is in the IV$^{th}$ (II$^{nd}$) quadrant for upward (downward) energy band bending with respect to the bulk at the position where it arises. Following the discussion from Sec. 5.1.2., one can see that in the case of non-linear recombination regime increasing the generation rate $\alpha\Phi$ will not only increase the magnitude of the SPV vector, but will also rotate it anticlockwise. Eventually, for very high $\alpha\Phi$ the SPV process will reach saturation, and consequently the SPV vector will become insensitive to changes in the generation rate.

This vector model is especially useful when more than one SPV formation processes occur in the spectrum run. A typical example is found in multilayered samples, where the absorption of the substrate and of the different layers usually results in SPV processes with different amplitudes and phases. Such situation can be modeled by considering the addition of a second SPV

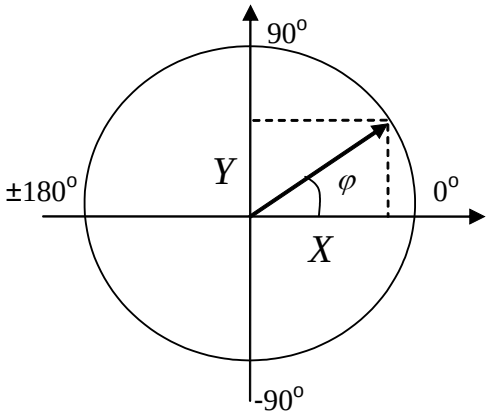


**Fig. 5.** Representation of the SPV signal with a radial vector. Reprinted with permission from [Ivanov, Ts., Donchev, V., Germanova, K., and Kirilov, K. J. Phys. D: App. Phys., 42, 135302, (2009)] Copyright IOP Publishing Ltd.

generation process (with amplitude $A_2$ and phase $\varphi_2$) to an already existing one (with amplitude $A_1$ and phase $\varphi_1$).

Let us first consider a system, which is and remains in linear recombination regime after the addition of the second process. If the phase difference $|\varphi_2 - \varphi_1|$ between the two SPV processes is less than 90° [acute angle or more precisely $|\varphi_2 - \varphi_1| < \arccos(-A_2/2A_1)$, which can be derived geometrically with the help of the cosine theorem], the addition of the second vector will result in a vector with larger magnitude, while if the angle is obtuse, the resulting magnitude will be smaller. In both cases the resulting vector will be rotated towards the second vector. Thus, both SPV amplitude and phase can change in both directions and one of the four possible combinations will take place, depending on the concrete amplitudes and phases of the two processes. Figure 6 illustrates different combinations of the magnitudes and angles of the two SPV vectors and their effect on the resulting SPV vector.

If one of the SPV generation processes involves non-linear recombination, the overall SPV phase spectral behavior is influenced by both the appearance of a second process (which can change the phase in both directions) and the non-linearity of the process (which changes the phase only in anticlockwise direction with increasing $\alpha\Phi$, as discussed above).

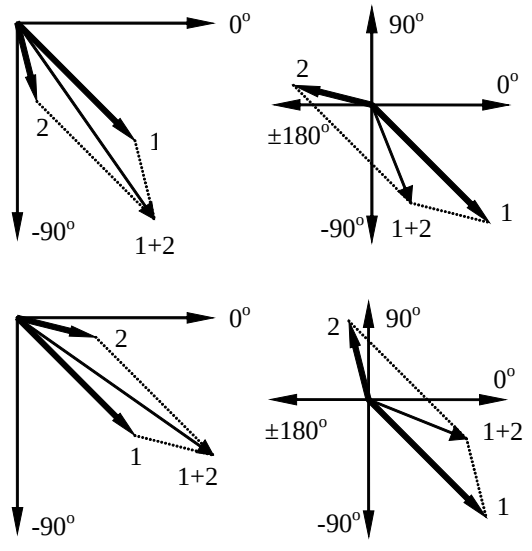


**Fig. 6.** Different combinations of the magnitudes and angles of the two SPV vectors ("1" and "2"), leading to change in magnitude and orientation of the resulting overall SPV vector ( "1+2") with respect to vector 1.

In this sense, in some cases, depending on the concrete values of $\alpha\Phi$, the bandgap-related step in the $\varphi(h\nu)$ spectrum (which changes φ in anticlockwise direction) could be due to two effects: i) the inclusion of the SPV vector, corresponding to the band-to-band absorption and ii) its rotation in anticlockwise direction, due to the gradual transition of the system in non-linear recombination regime.

We emphasize that the measurement gives the SPV signal, corresponding to the resulting overall vector (the vector sum of the vectors representing all the active processes) and deriving information about the individual processes requires further efforts. A quantitative analysis of the SPV vector addition requires assuming that the two processes are independent, which is a prerequisite for the validity of the superposition principle. As in the general case this is not strictly accomplished, we focus here only to the qualitative analysis. Nevertheless, there are many cases in practice, where the dependence between the different processes is very weak and can be neglected. For example, the absorption of a thin QW leads to reduced photon flux density reaching the substrate and this way alters the substrate related SPV process. However, because of the huge difference between the QW and substrate volumes, this influence is small and could be neglected, especially in the case of non-linear recombination and saturation of the processes in the substrate. So, in similar cases quantitative calculations with the vector model will be possible and justified.

## 6. Applications of the SPS for characterization of semiconductor nanostructures

### 6.1. Brief overview of the SPS studies of nanostructures performed in the last decade

This section provides a brief overview of the SPS applications for characterization of nanostructures containing single (or multi-) QWs, regular SLs, QDs and nanorods. Information about SPS of such nanostructures is presented in the excellent reviews of Kronik and Shapira [1, 2], but they

cover the works performed in the nineties of the 20th century. Here we consider studies devoted to this problem carried out mainly in the last decade of the current century. To our knowledge no complete description of these studies has been published. On the other side, such an overview provides a good basis to outline our works, which are the main subject of the present review. We believe they belong to the latest achievements in this quickly developing field.

**6.1.1. SPS of quantum wells and superlattices**

One of the first SPV investigations of QWs and SLs have been carried out by the group of Shapira and Ashkenasy in the 90s of the 20th century. By means of the Kelvin probe method these authors have studied various GaAs/AlGaAs based QWs and SLs. Using the sign of the SPV spectral steps they have constructed the band diagram of the investigated structure including the band bending at the interfaces [44]. The carrier effective lifetime in a GaAs QW situated in a p-i-n structure has been assessed in [45] and it has been shown that the SPV signal should increase with decreasing the well width. Further, they have observed the ground and excited states transitions in the SPV spectrum of a laser structure, containing an $In_{0.15}Ga_{0.85}As/GaAs/Al_xGa_{1-x}As$ QW [46]. This has allowed assessing the built-in electric field around the QW and the laser emission wavelength.

The group of F. Koch has demonstrated an original SPV based method for determining the band offsets $\Delta E_v$ and $\Delta E_c$ in QWs, which is applicable to type I as well as to type II interfaces [47]. Its advantage is that one and the same sample is used to determine both $\Delta E_v$ and $\Delta E_c$, contrary to the capacitance based methods, where two samples with different conductivity types are necessary.

In 2001 Datta *et al.* have proposed the so called *soft contact SPV* measurement method [48], in which the probe electrode is a glass, covered by a conductive transparent indium-tin-oxide (ITO) film. The electrode gently presses the sample surface while illuminating by chopped light. The authors have demonstrated a huge increase of the SPV signal from $In_{0.26}Ga_{0.74}As/GaAs$ QWs [48] as compared to the conventional SPV. From the temperature dependence of the SPV, PL and photoconductivity spectra they have concluded that the main mechanisms for carrier extraction from the QW are the thermal escape and the field assisted tunneling. The same conclusions are derived also by Dumitras *et al.* [18].

In their theoretical work [42] H. Ruda and A. Shik have derived an expression for the SPV signal of a semiconductor structure containing one or a few QWs in the SCR, considering the cases of linear and non-linear recombination regime. The authors have shown that for $h\nu$ lower than the barrier bandgap the SPV spectrum is proportional to the QW absorption spectrum including the excitonic peaks, while for $h\nu$ above the barrier bandgap the signal reveals a sharp increase followed by a constant value.

Wang *et al.* [25] have carried out SPS studies of GaAs/AlAs multi-QWs and have observed the QW related spectral structures as deeps superimposed on the substrate associated background. The net contribution of the QWs is obtained by subtracting the SPV spectra of the MQW structure and the bare GaAs substrate. The spectral deeps are explained by the decrease of the photon flux reaching the substrate due to the QW absorption. Unfortunately the authors don't give any discussion about the spectral behavior of the SPV phase, which would be useful for obtaining a deeper understanding of the experimental observations.

In a number of papers SPS studies on vertical cavity surface emitting lasers structures based on GaAs/AlGaAs, InGaAlAs/InP and InGaAs/GaAs/AlGaAs have been carried out. Temperature [49-51], angle [50-53] and polarization [54] dependences of the SPV spectra have been reported, which reveal the features related to the QW and the cavity. Valuable information has been retrieved about the QW width, the chemical composition and the quality of the samples. Differential SPV spectroscopy has been also applied by these authors [51, 53] in order to increase the sensitivity and the accuracy of the measurements.

In recent years the application of the SPS extends towards more complicated QW systems. For example by means of SPS and photoreflectance

spectroscopy of $GaAs_{1-x}Sb_x$/GaAs multi-QWs, combined with EFA electronic structure calculations Sitarek *et al.* [55] have shown the existence of weak type-I band alignment in the samples. Fox *et al.* [21] have studied by SPS tri-metal quaternary InGaAlAs QW laser structures, grown on InP, designed to emit at 1.55 μm. It has been found that the trimetal samples have a much larger conduction band offset of ~66% as compared to the ~40% in the conventional InGaAsP QW sample, which makes the former more suitable for semiconductor lasers with respect to improved thermal performance and potential wavelength range.

Sharma *et al.* have realized *Fourier Transform Infra Red (FTIR) Surface Photovoltage Spectroscopy* [56], employing a FTIR spectrometer, in which the detector was replaced by the sample mounted in the MIS geometry. This way information about the ground and excited state transitions in a GaInSb/AlGaInSb QW laser at room temperature was obtained, which was not possible by means of other techniques.

### 6.1.2. SPS of quantum dots

Bhattacharyya *et al.* [6] have observed the ground and the first three excited state transitions in InAs/GaAs QDs arranged in two layers embedded in a n-i-p structure. The SPV spectra have revealed light polarization dependence. This result was accounted for by the calculation of the optical absorption spectrum in frames of the EFA considering a rectangular potential well along the growth axis and an anisotropic 2D parabolic potential in the QD plane in accordance with atomic force microscopy (AFM) results.

Touskova *et al.* [15] have studied single and multi-layer InAs/GaAs QD. The broad features observed in the SPV spectra were explained by the broad QD size distribution (20-100 nm) obtained by AFM. The performed analysis has shown that the QD size in the multi-layer structures increases with decreasing the spacer thickness as well as with increasing the number of the layers. These results were explained by the stress accumulation, leading to growth of larger QDs.

A number of papers devoted to SPV studies of multi-layered InAs/GaAs QDs structures have been published by C. H. Chan and coworkers. In [57] these authors have investigated the effects of decreasing the GaAs spacer thickness. The increased electronic interaction between adjacent layers leads to miniband formation and red shift of the optical transition energies. However for very thin spacers (10 and 5 nm) the increased structural interaction between the QD planes changes the strain distribution and favors material interdiffusion, which results in blue shift [58]. The authors have stressed also that the SPV spectrum reveals more structures than the PL one that shows only the peak of the ground state transitions [24]. The temperature dependence of the QD SPV signal has revealed a maximum at intermediate temperatures [58]. The decrease at higher temperatures has been explained by phonon scattering of the photocarriers, while that at lower temperatures – by the hampered carrier thermal extraction from the QD potential wells.

The potential of the SPV spectroscopy as an useful tool for studying carrier tunneling and vertical coupling between multi-layered quantum dots has been demonstrated also by Malikova *et al.* [22] for CdSe/ZnCdMgSe QDs using the so called Kelvin Force Microscopy (KFM) [59] with a resolution of 100 nm.

Sharma *et al.* [23] have performed a detailed study of InAs/InGaAs/InP QDs designed for lasers emitting around 2μm. Information about the QD ground and excited states has been obtained by means of complementary spectroscopic techniques - PL, SPV and photoreflectance, performed on one and the same spot on the sample surface at different temperatures.

### 6.1.3. SPS of nanorods and nanowires

The group of D. Wang has performed a number of SPS studies of ZnO nanorods fabricated on conductive ITO substrates in aqueous solution [60-63]. The effect of the ethanol and the liquid-crystalline porphyrin [63] as well as of the absorbed oxygen [62] on the ZnO photovoltaic properties has been investigated. More complicated structures such as $ZnFe_2O_4$ nanotube arrays [64] and ZnO nanowire arrays coated with CdS QDs [20] have been also examined.

### 6.2. SPS of AlAs/GaAs SLs with GaAs embedded QWs with graded interfaces

Short-period AlAs/GaAs SLs with GaAs embedded QWs have currently received considerable interest [65]. They show a number of new physical properties often different from those of single QWs and unperturbed SLs. Besides they have many advantages in comparison with single GaAs QWs with homogeneous AlGaAs alloy-like barriers [65]. That is why these complicated nanostructures are very interesting for both basic research and advanced device fabrication [65, 66]. Thus, the study of their electronic and optical properties, as well as the effect of the interface grading, by means of different experimental and theoretical methods is a problem of both fundamental and applied importance. A detailed PL and theoretical study of these nanostructures is presented in our previous paper [65]. However to the best of our knowledge their characterization by means of SPS was not reported before our pioneering works [7-10], which are devoted to this interesting problem.

#### 6.2.1. Experimental details

The following samples have been studied:

i) Samples grown by MBE at 600°C on n-type (100) GaAs substrates doped at a level of $1\times10^{18}$cm$^{-3}$. After a 400 nm GaAs buffer layer an $(AlAs)_4/(GaAs)_8$ SL is grown [4 and 8 denote the number of AlAs and GaAs monolayers (MLs), respectively; 1ML = 0.283 nm] which contains two GaAs EQWs (12 and 5 nm wide). There are 5, 24 and 20 periods of SL below the 12 nm EQW, between the two EQWs and above the 5 nm EQW, respectively. A 30 nm $Al_{0.33}Ga_{0.67}As$ cap layer terminates the structure [7].

ii) Samples grown by MBE at 600°C on two types of substrates: n-type (100) GaAs:Si ( $1\times10^{18}$ cm$^{-3}$) and semi-insulating (SI) (100) GaAs. They represent one GaAs QW of 5 nm (18 MLs) embedded between 20 (on top) and 26 (on bottom) periods of $(AlAs)_4/(GaAs)_8$ SL. There is a 50 nm cap layer of $Al_xGa_{1-x}As$ ($x$ = 0.33, which is the mean Al content in the SL). No buffer layer is grown between the substrate and the first SL [9].

In the samples grown on n-type GaAs, the energy bands in the structure are bent upwards with respect to the bulk, because the substrate is highly n-type doped and the rest of the structure is nominally undoped. Thus, a SCR with a built-in electric field occurs at the interface between the substrate and the structure. As the electric field in the substrate is effectively screened by the free electrons, the SCR develops rather in the structure than in the substrate. Hence, the GaAs buffer layer, the SL, the EQWs and the AlGaAs cap layer are situated in a region with an electric field.

iii) Bulk p-type and n-type Si samples with free surfaces. Prior to measurements the n-type sample has been treated with a chemical procedure, which produces a stable depleted SCR as described in [10, 41]. No treatment is performed for the p-type sample, since the free surface of p-type Si is known to be depleted in thermal equilibrium. The *p*-type (*n*-type) samples are cut from a Wacker wafer with a resistivity of 50 Ω.cm (5 Ω.cm), which corresponds to a free carrier concentration $p \approx 3\times10^{14}$ cm$^{-3}$ ($n \approx 9\times10^{14}$ cm$^{-3}$).

#### 6.2.2. SPV amplitude spectroscopy

##### Main features of the SPV spectrum

A typical SPV spectrum of a sample, depicted in Sec. 6.2.1.i) is presented by curve 1 in Fig. 7. It is recorded with the $SnO_2$ film probe in the soft-contact SPV mode using a photon flux density $\Phi = 4\times10^{13}$cm$^{-2}$s$^{-1}$. The spectral resolution was ±2.5 nm. In this spectrum the following features can be seen: i) a step A with inflection point energy of 1.421eV; ii) two peaks at 1.458 eV (B) and 1.469 eV (C) situated at the beginning of a step, which follows step A; iii) two peaks at 1.579 eV (D) and 1.616 eV (E) situated at the beginning of another step; and iv) three further steps with inflection point energies 1.741 eV (F), 1.794 (G) and 1.815 eV (H), respectively.

The steps A (1.421 eV) and H (1.815 eV) correspond to the onset of the band-to-band absorption in the bulk GaAs (buffer layer and substrate) and in the AlGaAs cap layer, respectively. Their slightly lower energies compared to the nominal band-gaps (1.423 and 1.829 eV [67] respectively) are due to the Franz-Keldysh effect.

The experimentally obtained energy positions of the SPV spectral features B-G are given in the 3$^{rd}$ column of Table 1. In order to interpret these

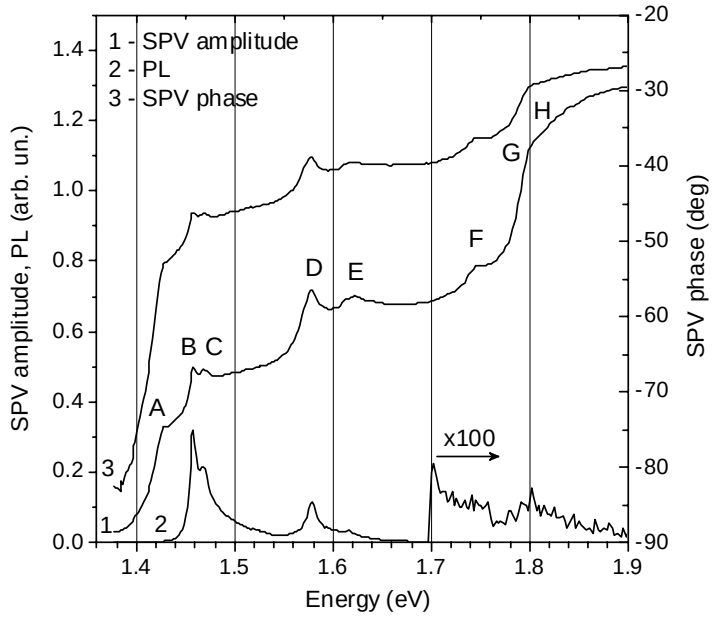


**Fig. 7.** Typical soft-contact SPV amplitude (curve 1), SPV phase (curve 3) and PL (curve 2) spectra, of a sample containing two GaAs quantum wells embedded in an AlAs/GaAs superlattice. The PL spectrum for energies higher than 1.7 eV is multiplied by a factor of 100.

**Table 1.** Optical transitions and their energies (in eV) as determined by SPS, PL and EFA calculations taking into account an interface grading, corresponding to a diffusion length of 3.7 ML (1.05 nm). The exciton binding energies are given in column 6 in meV. The last column represents the calculated values corrected for excitonic effects.

| Transition | Label | SPS | PL | EFA calculations ( $L_D$ = 1.05 nm ) | | |
|---|---|---|---|---|---|---|
| | | | | | $E_{exciton}$ | $E - E_{exciton}$ |
| 1 | 2 | 3 | 4 | 5 | 6 | 7 |
| HH1-E1 (12 nm EQW) | B | 1.458 | 1.458 | 1.462 | 9 | 1.453 |
| LH1-E1 (12 nm EQW) | C | 1.469 | 1.468 | 1.475 | 10 | 1.465 |
| HH1-E1 (5 nm EQW) | D | 1.579 | 1.579 | 1.594 | 12 | 1.582 |
| LH1-E1 (5 nm EQW) | E | 1.616 | 1.618 | 1.628 | 13 | 1.615 |
| HH3 – E3(12 nm EQW) | F | 1.741 | …. | 1.748 | 9 | 1.739 |
| HH3 (12 nm EQW) - E(SL) | F | 1.741 | …. | 1.757 | 9 | 1.748 |
| HH(SL) - E(SL) | G | 1.794 | 1.802 | 1.817 | 4 | 1.813 |

features we have compared their energy positions with the optical transition energies calculated theoretically in frame of the EFA, neglecting the electric field. As the real interfaces are not abrupt due to the intermixing of the material components [68], we take into account the possible interface grading effects.

In the calculations of the bound states we consider a model structure very similar to the real one, described in Sec. 6.2.1.i). The interface grading is represented by interdffused concentration profile [65, 69]. This way the interfacial potential becomes graded, too. The diffusion length $L_D$ is a parameter, determining the degree of interface

grading. The one-band EFA equation is solved numerically by the finite differences method for potential profiles corresponding to different $L_D$ values. The material parameters are taken from [67]. The 5th column of Table 1 presents the calculated optical transitions energies assuming an interface grading corresponding to a diffusion length of 3.7 MLs (1.05 nm). This value is in accordance with previous finding for similar samples by PL measurements [65]. For the exciton binding energies of the EQWs we use the values calculated in [70] for a GaAs/AlAs/AlGaAs QW with double barrier. They are listed in the 6th column of Table 1. The SL exciton energy is taken to be 4 meV [71]. The last column gives the calculated transition energies, corrected for excitonic effects. They are more relevant compared to the results presented in [65, 69], which consider simpler model structures. The distinctions with respect to the previous calculations are more noticeable for states with higher energies. In particular, the SL minibands obtained in the present calculations are wider and better corresponding to the SL energy spectrum of the real structure.

The comparison between the 3rd and the last column of Table 1 reveals a very good agreement of the experimental and the theoretical transition energies. This enables us to explain the SPV spectral features B-G as follows. The peaks B (1.458 eV) and C (1.469 eV) are identified as the heavy-hole (HH) and light-hole (LH) exciton peaks of the 12 nm EQW. The peaks D (1.579 eV) and E (1.616 eV) are identified as the HH and LH exciton peaks of the 5 nm EQW. The two steps, which start with the peak doublets B-C and D-E, correspond to the two-dimensional joint density of states in the 12 nm and 5 nm EWQs, respectively.

The interpretation of step F (1.741 eV) is based on the following considerations. The experimental energy is very close to the calculated one for the HH3-E3 transition in the 12 nm EQW (1.739 eV). However, if this transition was the sole origin of step F, the latter would be manifested as an exciton peak similar to peaks B-E, rather than as a step. Further we have found that the transitions between the HH3 state of the 12 nm EQW and the lowest states in the SL electron miniband are also close in energy to step F (see Table 1). Moreover, our calculations have shown that the SL electron states (in particular the ones originating from the 25 period SL) penetrate in the 12 nm EQW. This is a manifestation of the interaction between the SL and the EQW, which is due to the fact that the E3 state energy is very close (9 meV) to the SL miniband (see [65] for a detailed discussion). As a result an increased probability exists for mixed optical transitions between the HH3 state of the 12 nm EQW and the states in the SL electron miniband. Because the SL states are closely spaced in energy, such transitions will result in a step like structure. Thus, we have ascribed step F to both the HH3-E3 transition in the 12 nm EQW and a mixed transition between the HH3 state of the 12 nm EQW and the SL electron miniband. The step G (1.794 eV) is due to the E-HH exciton and free carrier transitions in the SL (see Table 1).

The conclusions given above are supported by PL measurements. The room temperature PL spectrum of the investigated nanostructure is shown by curve 2 in Fig. 7. Comparing curves 1 and 2 one can see that within the experimental error (~4 meV) the SPV peaks from B to E have the same energy positions as the four PL peaks originating from the HH and LH excitonic transitions in the two EQW [65].

The comparison between the SPV and PL spectra also shows that the SPS is more informative than the PL spectroscopy. Indeed the structures F and H are not seen in the PL spectrum. Only a week and noisy bump, corresponding to the PL of the SL, is observed around 1.8 eV after magnification by a factor of 100. Besides, the LH exciton peak E (1.616 eV) of the 5 nm EQW is better resolved in the SPV spectrum. The last results are not surprising having in mind that the SPS reflects the spectral behavior of the optical absorption coefficient [1, 6, 18], while the PL reveals the emission properties, which are dominated by the lowest energy levels and limited only to the radiative recombination processes.

**Carrier escape from the EQW**

The photogenerated carriers must be separated by the built-in electric field in the sample in order to give rise to a SPV signal. Previous studies on QWs have shown that the separation of carriers into the QW itself plays insignificant role in the

SPV generation process [17, 18]. The main contribution to the SPV signal comes from carriers escaped from the QW, because they can separate over longer distances [18]. The photocarrier escape mechanisms at room temperature from InGaAs/GaAs QWs situated in the SCR are proven to be thermal emission and field-assisted tunneling emission [17, 18]. In our samples the QWs are surrounded by SLs and thus the energy barriers for carrier escape are the differences between the bound states of the EQWs and the corresponding SL electron or hole miniband. Our EFA calculations have shown that these barrier energies are of the same order of magnitude or lower than the emission barrier energies in single GaAs/$Al_{0.33}Ga_{0.67}As$ QWs with the same well widths. The electron and hole escape times from similar single GaAs/AlGaAs QWs at 300K are much shorter (less than 1 ns [72]) than the period of our light modulation (~ 0.01s), which implies that the carrier escape rate from the EQWs is not a limiting factor for the SPV signal. According to the above discussion we assume that in the samples under study the photogenerated carriers in the EQW escape towards the SL minibands via thermal emission and field-assisted tunneling emission as in single QWs [17, 18].

**Carrier transport in the superlattice**

Carrier transport in the SL of the investigated structure is another necessary condition for obtaining SPV signal. It is known that at large electric fields $F$ the SL miniband converges towards a series of discrete states spaced by $eFd$, where $d$ is the SL period (Wannier-Stark effect [73]). However at low electric fields, where $eFd$ is much smaller than the SL miniband width, the coupling between SL wells is preserved and carriers move along the growth direction through resonant tunneling in the minibands. A rough estimate of the built-in field in our structure gives $F \approx 10^4$ V.cm$^{-1}$. Taking into account the SL period $d$ = 3.4 nm (12 ML) we obtain $eFd \approx 3.4$ meV. This value is much smaller than the widths of the SL minibands found in the EFA calculations, namely 263, 44 and 157 meV for electrons, HH and LH, respectively. Consequently the splitting of the SL minibands in our samples plays insignificant role and the photocarrier transport in the SL occurs in the low electric field regime through resonant tunneling in the SL minibands. Due to the built-in electric field the photocarriers in the minibands are separated in space – the holes move towards the surface and the electrons move towards the bulk, thus generating SPV signal. Carrier capture and reemission processes by the EQWs are also possible - the 5 nm EQW can capture and reemit holes escaped from the 12 nm EQW, while the 12 nm EQW can capture and reemit electrons escaped from the 5 nm EQW.

**Photon flux dependence of the SPV signal from the EQWs**

Further we have measured the dependence of the SPV spectrum on the photon flux density. The net contributions to the SPV signal of the HH excitonic transitions in the two EQWs were estimated by subtracting the substrate related signal from peak B (12 nm EQW) and the contribution of the substrate and the 12 nm EQW from peak D (5 nm EQW). The results for the 12 nm EQW (peak B) show a power law dependence with a coefficient $\beta$ = 0.51 up to the maximal photon flux density $\Phi_{max} = 5\times10^{14}$ cm$^{-2}$s$^{-1}$. For the 5 nm EQW (peak D) a satisfactorily fit is obtained in the range $\Phi \leq \sim 0.3\Phi_{max}$ ($1.5\times10^{14}$ cm$^{-2}$s$^{-1}$) with $\beta$ = 0.46, while for larger $\Phi$ the experimental dependence becomes weaker. More details can be found in [7]. These findings are in agreement with the theoretical predictions of Ruda and Shik for isolated QWs [42]. Taking into account that with respect to the SPV signal generation the only distinction between the EQW and the isolated QW are the SL barrier regions, this result could be considered as a further experimental confirmation of the theoretical model developed in [42].

In summary of Sec. 6.2.2.: SPS investigations of short-period AlAs/GaAs SLs containing two differently wide GaAs EQWs with graded interfaces have revealed the free exciton transitions in the EQWs and in the SL. This has been confirmed by PL measurements and EFA electronic structure calculations. It is to be noted that contrary to other SPS studies of QWs [17, 18], the EQW and the SL electronic transitions in our samples are more difficult for monitoring, because they occur over a background due to the substrate absorption. Nevertheless our SPV spectra have revealed well resolved structures, which nature has been properly explained. Further, it has been shown that the carrier escape from the EQW is realized

via thermal emission and field-assisted tunneling and that their transport in the barrier regions occurs in the low-electric-field regime through resonant tunneling in the SL minibands. Besides, the investigation of the photon flux dependence of the SPV signal has confirmed the theoretical model developed in [42].

### 6.2.3. SPV phase spectroscopy

In this Section is demonstrated the applicability of the conclusions derived in Sec. 5.1.

#### SPV phase and energy band bending

The samples depicted in Sec. 6.2.1.iii) are measured. Figures 8 and 9 represent the SPV amplitude and phase spectra, respectively, recorded in the p-type and n-type Si samples for three light modulating frequencies with $\Phi \approx 8 \times 10^{14}\ cm^{-2}s^{-1}$. The SPV amplitude spectra of the two types of samples (Fig. 8) are similar. Looking only at these spectra it is difficult to guess the type (p or n) of the semiconductor. This becomes possible if one considers the SPV phase spectra (Fig. 9). The SPV phase spectrum of the p-type (n-type) sample with downward (upward) surface band bending reveals a bandgap-related knee around 1.1 eV, corresponding to a shift of φ towards 180° (towards −0°). This result is in full agreement with the discussion given in 5.1.1.

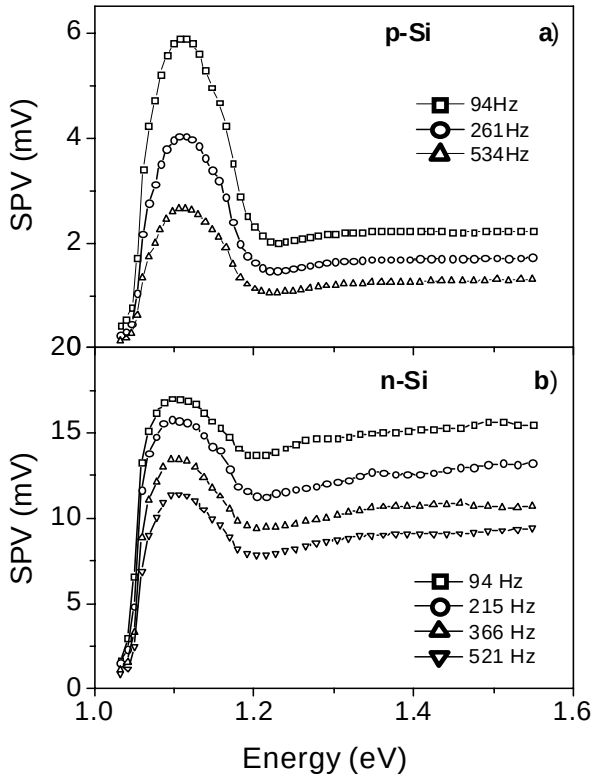


**Fig. 8.** Surface photovoltage amplitude spectra, recorded in p-Si (a) and n-Si (b) for different light modulating frequencies indicated on the figure. Reprinted from [Donchev, V., Kirilov, K., Ivanov, Ts., and Germanova, K. Mat. Sci. & Engineering B, 129 (1-3), 186-192. "Surface photovoltage phase spectroscopy – a handy tool for characterisation of bulk semiconductors and nanostructures"] Copyright (2006), with permission from Elsevier.

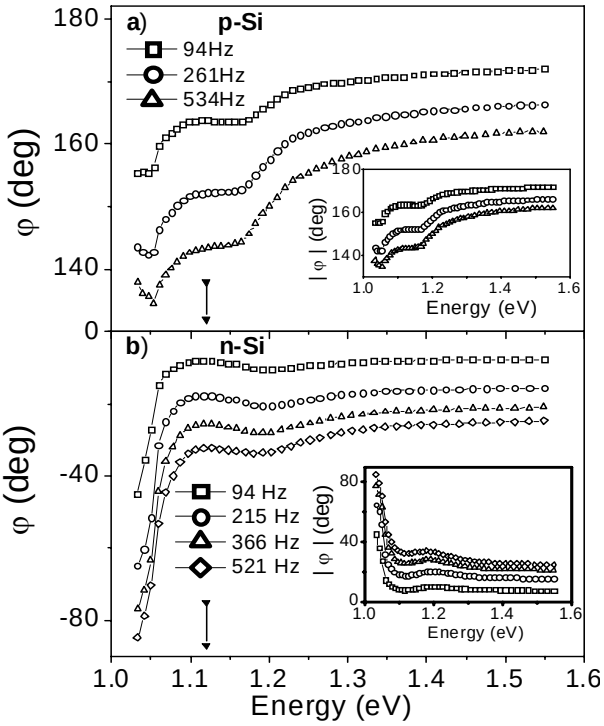


**Fig. 9.** Surface photovoltage phase spectra, recorded in p-Si (a) and n-Si (b) for different light modulating frequencies indicated on the figure. The arrows designate the energy of the Si bandgap. Note that with increasing hν the phase modulus increases in (a) and decreases in (b) as shown in the insets. Reprinted from [Donchev, V., Kirilov, K., Ivanov, Ts., and Germanova, K. Mat. Sci. & Engineering B, 129(1-3), 186-192. "Surface photovoltage phase spectroscopy – a handy tool for characterisation of bulk semiconductors and nanostructures"] Copyright (2006), with permission from Elsevier.

It is seen also from Fig. 9 that increasing the light modulation frequency changes φ in clockwise direction, i.e., increases the SPV phase retardation. This is in agreement with the theoretical calculations and experimental results presented in other works [39-41].

**SPV phase and optical absorption coefficient**

The samples depicted in Secs. 6.2.1.i) and 6.2.1.iii) are measured. The experiments are carried out at intermediate values of the photon flux, where a deviation from the linear recombination regime is present at least for super-bandgap excitation. As explained in Sec. 5.1.2., a decrease of the SPV phase retardation with increasing $\alpha(h\nu)$ (increasing $h\nu$) is expected.

Indeed one can see from Fig. 9(a) and (b) that with increasing $h\nu$ the SPV phase, measured at a fixed frequency, changes anticlockwise. This behaviour is observed not only as a bandgap-related knee, but also for larger energies ($h\nu$ > 1.18 eV), where $\alpha(h\nu)$ further increases.

The fact that φ depends on $\alpha(h\nu)$ could be useful in the SPV characterisation of nanostructures, where the light absorption spectrum in the supper-bandgap region reveals sharp maxima, corresponding to excitonic transitions between bound electron and hole states. According to the considerations presented in Sec. 5.1.2., the absorption coefficient maxima in a QW are expected to be observed also in the SPV phase spectrum as positive peaks, corresponding to anticlockwise rotation of φ, i.e. to a reduction of the phase retardation. This holds if the photocarrier escape from the QW is a sufficiently fast (with respect to *f*) process, which introduces no substantial shift in the SPV phase. At the frequencies used in our experiments this assumption is fulfilled, taking into account that at 300K the escape times for electrons and holes from GaAs/AlGaAs QWs are less than 1 ns [72].

Curve 3 in Fig. 7 (Sec. 6.2.2.) presents the SPV phase spectrum, corresponding to the amplitude one (curve 1). We emphasize that the structures A-H observed in the amplitude spectrum (curve 1), are well resolved also in the SPV phase spectrum (curve 3), where they appear at the same energy positions. The observation of well resolved optical absorption coefficient spectral features in the SPV phase spectrum strongly supports the above developed idea about the relation between the SPV phase and the optical absorption coefficient. We have found also that under certain experimental conditions the exciton transitions are even better resolved in the SPV phase than in the SPV amplitude spectrum.

The knee in SPV phase spectrum (curve 3), related to the onset of the bulk GaAs band-to-band optical transitions (~1.421 eV) corresponds to a phase change towards $-0^{o}$. The phase change corresponding to the observed exciton absorption peaks of the two QWs is in the same direction. Applying the approach, presented in Sec. 5.1.1., to the investigated multilayered structure leads to the conclusion that the energy bands are bent upward towards the sample surface. This finding is in accordance with the discussion, given in Sec. 6.2.1.

### 6.2.4. Application of the vector model for simultaneous analysis of the amplitude and phase SPV spectra

In this section are given the basic results [9], concerning the development of an original vector model for the representation of the SPV signal (Sec. 5.2.). In order to demonstrate the efficiency of the model we have measured SPV amplitude and phase spectra of the EQW samples, depicted in Sec. 6.2.1.ii). The application of the vector model has allowed us to understand and explain their complicated and intriguing behavior, which has provided useful information about the investigated structures.

As mentioned in Sec. 6.2.1.ii) the samples used in this study are identical structures, which are grown on two different types of substrates. The measurements are performed with the $SnO_2$ film probe in the soft-contact SPV mode keeping the photon flux density constant ($1\times10^{13}cm^{-2}s^{-1}$ ± 0.5%) by means of the neutral density filter method. The spectral resolution was ±5 nm.

**Samples grown on n-GaAs substrates**

Figure 10 displays typical SPV amplitude and phase spectra of these structures. The amplitude spectrum has been studied in our previous work [8], where all the spectral features have been

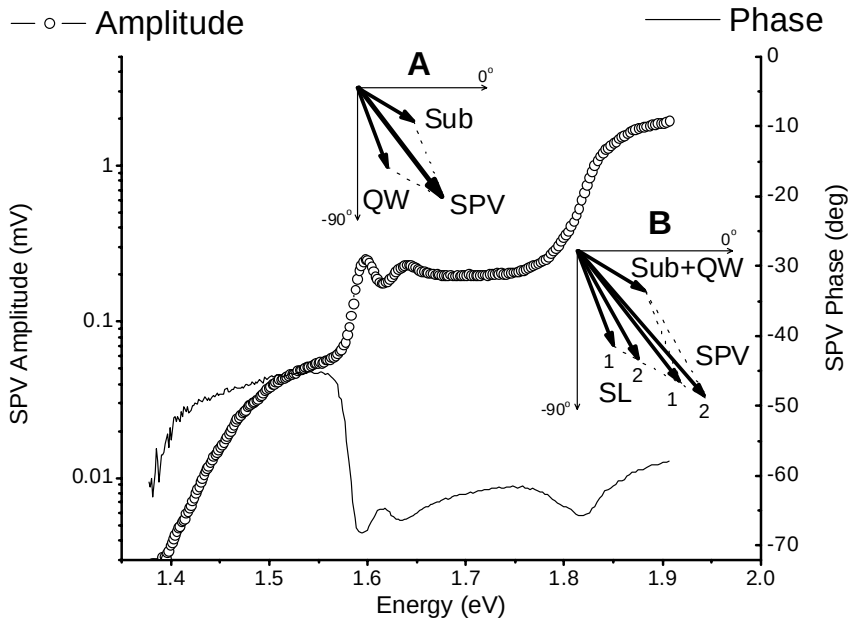


**Fig. 10.** SPV amplitude (open circles) and phase (solid line) spectra of a sample grown on $n^+$- type substrate. Insets A and B – vector diagrams showing the interaction of different SPV processes for two different spectral regions**.** Sub, QW and SL denote the substrate, QW and SL vectors. Reprinted with permission from [Ivanov, Ts., Donchev, V., Germanova, K. and Kirilov, K. J. Phys. D: App. Phys., 42, 135302, (2009)] Copyright IOP Publishing Ltd.

identified based on comparison with PL investigations and EFA calculations.

The step in the range 1.400 – 1.550 eV in the amplitude spectrum (Fig. 10) originates from transitions in the GaAs substrate ($E_g$=1.424 eV). In agreement with [10] and the discussion given in Sec. 5.2., its n-type doping leads to an SPV vector in the $IV^{th}$ quadrant ($\varphi$ is around -50°). With increasing the light energy the SPV amplitude increases due to the increased absorption. Simultaneously the SPV phase is almost constant in accordance with the linear dependence of the SPV signal on the photon flux density in this range [see Fig. 12(a)]. Around 1.550 eV, both SPV amplitude and phase reach a nearly constant value, which is in accordance with the calculations and experimental results of other authors [42, 74]. The relatively low substrate contribution to the SPV is due to the high Si doping, which effectively screens the electric field and leads to a very narrow SCR situated mainly in the SL structure.

Above 1.550 eV the QW starts to absorb and its contribution to the SPV signal can be represented by a second vector again in the $IV^{th}$ quadrant [10], due to the above depicted energy band bending in the nanostructure. As the overall SPV vector in this range experiences a clockwise rotation ($\varphi$ decreases, see the solid line in Fig. 10), from the vector model follows that the QW vector is closer to -90° than the vector of the substrate (see inset A, Fig. 10). This means that the SPV process from the QW is slower as compared to the SPV process in the substrate. The amplitude spectrum in this range reveals two peaks ascribed to the E1-HH1 (1.597 eV) and E1-LH1 (1.639 eV) free exciton transitions in the QW similar to [8]. Accordingly, the SPV phase also exhibits two dips at very close energies (E1-HH1 at 1.593 eV and E1-LH1 at 1.635 eV), corresponding to clockwise rotation. The small difference of the energy positions (4 meV) of these features between the amplitude and phase spectrum can be explained by a slight anticlockwise rotation of the QW vector in addition to its magnitude change. Following the discussion in Sec. 5.2., this rotation is in accordance with the slightly non-linear dependence of the QW related SPV amplitude on

the photon flux density shown in Fig. 12(a). After the peaks, the SPV amplitude has a constant value, which reveals the 2D density of states in the QW. Accordingly the SPV phase also remains nearly constant in this range.

Above 1.750 eV a step in the SPV amplitude spectrum is observed with an inflection point at 1.822 eV. This step is associated with transitions between the electron and hole mini-bands of the SL [8]. The phase of the overall SPV signal is again in IV$^{th}$ quadrant in accordance with the direction of the energy band bending [10]. It first shows clockwise vector rotation ($\varphi$ decreases) as in the QW region, but after 1.820 eV anticlockwise rotation starts ($\varphi$ increases), while the SPV amplitude increases throughout the whole range of the SL step. Applying the vector model we can explain this behavior in two stages. The initial rise in the SL absorption leads to rise of the SL vector's magnitude, which leads to clockwise rotation of the overall SPV vector similar to the QW absorption. After 1.820 eV the SL vector also starts to rotate anticlockwise and this leads to anticlockwise rotation of the overall vector. This behavior is illustrated in Fig. 10; inset B, where the overall SPV vector is represented for two subsequent SL vectors, following the above scenario. Near the end of the step (1.850 eV), the SL signal is one order of magnitude larger than the signals from the substrate and the QW and it dominates the spectrum. The large magnitude of the SL contribution suggests a gradual transition towards non-linear recombination regime, which could explain the above mentioned rotation of the SL vector. This hypothesis is supported by the observed sub-linear SPV dependence on the photon flux density, measured at 1.906 eV shown in Fig. 12(a).

**Samples grown on SI GaAs substrates**

Below we discuss the second set of samples, grown on SI GaAs substrates. Figure 11 shows typical SPV amplitude and phase spectra. Although the quantum structure is the same for both sets of samples, there is a big difference in the line-shape of the spectra. Figure 11 reveals dips in the amplitude and peaks in the phase spectrum, contrary to the samples with n-type substrates (see Fig. 10). At a first glance this result is unexpected. However, using the vector model and having in mind the properties of the substrate and the quantum structure we can explain this behavior as follows.

Because in SI GaAs the energy bands are virtually flat, the dominant cause for SPV generation in the substrate is the Dember voltage effect [4, 75], which relies on the difference in the carrier mobilities. Since the electrons diffuse faster than holes, it gives SPV phase in the IV$^{th}$ quadrant [1, 10]. The amplitude of the substrate signal is much larger as compared to the n-type GaAs substrate, reported on Fig. 10, and dominates the SPV in the whole spectral range. The peak in the amplitude spectrum at 1.424 eV could be due to absorption from shallow acceptor states to the conduction band [4], but it will not be discussed here. The quantum structure is nominally undoped, but as the most common residual impurity introduced during the MBE growth is carbon, one can expect a slight p-type doping (which effect for the other samples is masked by the high n-type doping of the substrate). Therefore the energy bands at the surface are bent downward with respect to the bulk. This means that the SPV processes generated from the QW and SL can be manifested by vectors in the II$^{nd}$ quadrant [10] (see also the discussion in Sec. 3). If these vectors form an obtuse angle with the substrate vector, like the one shown in the vector diagram in Fig. 11, the growth of their magnitude will result in a decrease in the magnitude and anticlockwise rotation of the overall SPV vector. This is the case for both, the QW and the SL spectral ranges, as can be seen from Fig. 11, where the SPV amplitude decreases and the SPV phase increases. Due to the large substrate signal, the contribution of the E1-HH1 exciton transitions in the QW is seen as a small dip in the amplitude and a small peak in the phase spectrum, both at 1.603 eV. The E1-LH1 exciton is observed at 1.643 eV in the inset of Fig. 11, where magnified amplitude and phase spectra are presented. The contribution of the SL is well resolved in Fig. 11, due to its larger volume – above 1.800 eV one observes a negative step in the amplitude and a positive step in the phase in accordance with the vector diagram in the inset of Fig. 11.

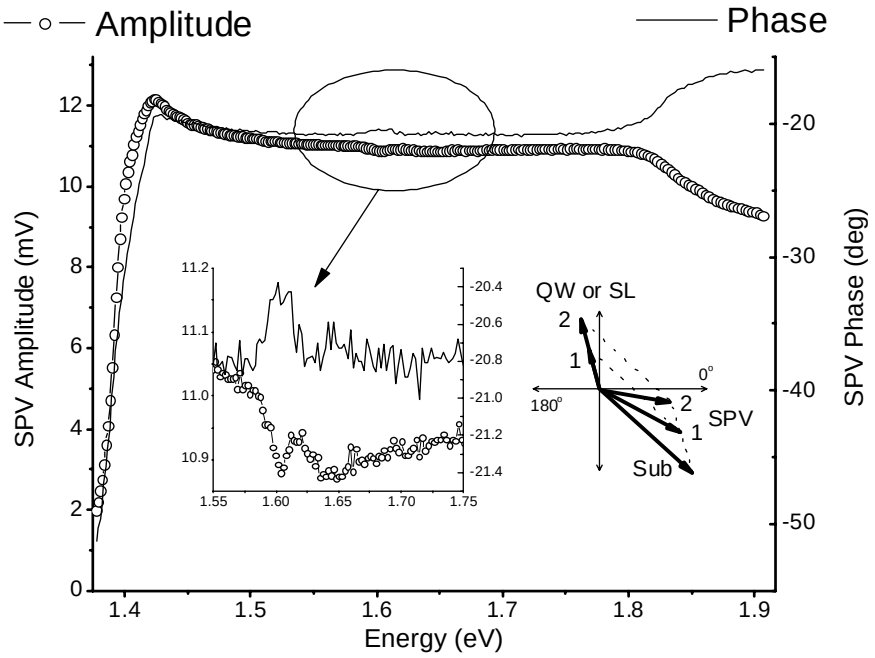


**Fig. 11.** SPV amplitude (open circles) and phase (solid line) spectra of a sample grown on SI GaAs substrate. Insets: magnified amplitude and phase spectra in the QW energy range; vector diagram showing the dependence of the overall vector on the growth of a vector in II$^{-nd}$ quadrant (QW or SL absorption). Reprinted with permission from [Ivanov, Ts., Donchev, V., Germanova, K., and Kirilov, K. J. Phys. D: App. Phys., 42, 135302, (2009)] Copyright IOP Publishing Ltd.

**Intensity dependence**

Finally we discuss the excitation density dependences of the major spectral features: substrate (1.530 eV), QW (1.599 eV) and SL (1.906 eV). Figure 12 shows how the SPV amplitude of these features changes with decreasing the photon flux density from its maximal value $\Phi_{max} = 1\times10^{13}$ cm$^{-2}$s$^{-1}$ used in the spectral runs from Figs. 10 and 11. The dependences obtained for the samples with Si-doped substrates [Fig. 12(a)] are in accordance with the SPV amplitude and phase spectral behavior, as discussed above. The dependences obtained for the samples with SI substrates [Fig. 12(b)] are strongly non-linear. The sub-linearity of the curve, corresponding to the substrate photon energy (1.530 eV) is expected, since the Dember voltage effect has a sub-linear dependence on $\Phi$ [4]. The contribution of the QW to the SPV signal is relatively small, so the dependence for the QW photon energy (1.599 eV) almost coincides with that of the substrate. At a first glance the excitation density dependence for the SL photon energy (1.906 eV) seems to contradict the intuition – reducing the photon flux density leads to increase in the SPV amplitude. Nevertheless it can be easily explained by the vector diagram in Fig. 11, assuming different excitation density dependences for the SL and substrate SPV processes. Indeed the substrate vector itself remains almost unchanged [confirmed by Fig. 12(b)] with decreasing $\Phi$, while the SL vector is expected to decreases. As the angle between these two vectors is obtuse, the net result is an increase of the overall SPV vector magnitude. At very low values of $\Phi$, the magnitudes of both vectors obviously decrease towards zero and so does the resulting SPV signal. An increase of the SPV amplitude with decreasing the excitation density has been observed in [4], but for sub-bandgap SPV features in bulk SI GaAs samples.

In summary of Sec. 6.2.4.: We would like to note that the presented results and their interpretation by means of the vector model have demonstrated its potential for the investigation of advanced semiconductor nanostructures.

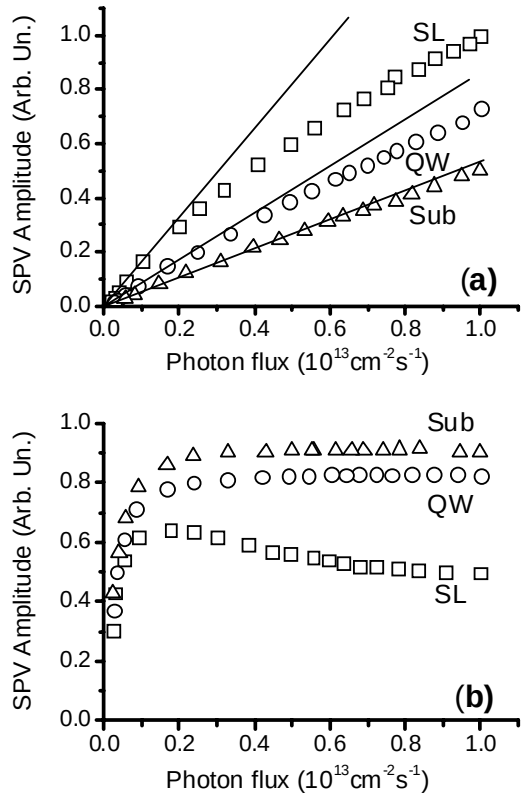


**Fig. 12.** Excitation density dependences of the major spectral features: Substrate (1.530 eV, triangles), QW (1.599 eV, circles) and SL (1.906 eV, squares) for samples grown on (a) n-GaAs and (b) SI GaAs substrates. The straight lines in a) are a guide for the eye. All curves are normalized to different values for clarity. Reprinted with permission from [Ivanov, Ts., Donchev, V., Germanova, K., and Kirilov, K. J. Phys. D: App. Phys., 42, 135302, (2009)] Copyright IOP Publishing Ltd.

## 6.3. SPS of self-assembled InAs/InP quantum wires

Multi-layer structures with self-assembled InAs/InP QWRs are promising candidates for light emitting devices in the 1.3 - 1.55 μm wavelength range used in optical fiber telecommunications [76]. The optical properties of InAs/InP QWRs have been studied mainly by low-temperature PL spectroscopy revealing several wide bands, which have been generally attributed to emission of QWRs belonging to different families having heights differing by an integer number of monolayers [26, 77, 78]. Calculations of the electronic structure have been performed using the EFA [77, 79]. Experimental investigations at room temperature, which will be the operating temperature of a final device, are relatively few, including Raman [27] and optical absorbance spectroscopy [80]. As the SPS reflects the optical absorption spectrum [1, 6, 7, 11, 18], it is an alternative to avoid the difficulties related to optical absorbance measurements in nanostructures. That is why we apply SPS to study multi-layer InAs/InP QWRs at room temperature in combination with PL measurements, structural data from previous studies [26], and comparison with ETB electronic structure calculations.

### 6.3.1. Experimental and calculation details

Four samples have been studied, grown on SI (001) InP:Fe substrates by solid-source molecular beam epitaxy at 515°C [26]. They contain a 150 nm InP buffer layer and a stack of seven InAs QWR layers, separated by InP spacers of thickness $d$ = 3, 5, 10 and 20 nm, respectively. Figure 13 shows a schematic of the sample structure. The buffer and the structure have an n-type residual doping of the order of $1\times10^{17}$ cm$^{-3}$. AFM has shown that the QWRs are oriented

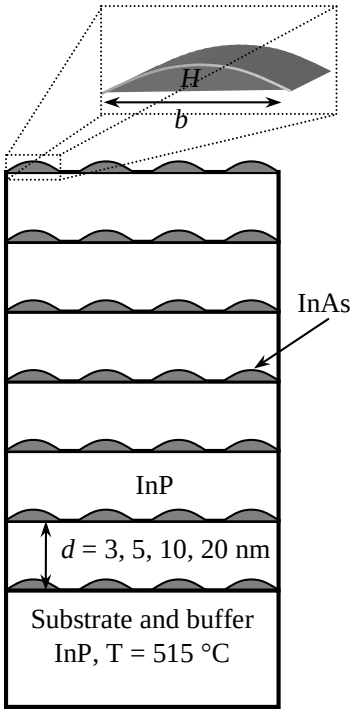


**Fig. 13.** A schematic of the sample structure. The grey (white) regions represent InAs (InP).

along [1-10] direction and their average height $H$ increases from 1.5 to 2.2 nm when $d$ decreases from 20 to 3 nm [26]. Both values are much smaller than the lateral QWR width $b$, which is of the order of 13 nm.

The SPS measurements are performed with the $SnO_2$ probe situated as close as possible to the sample surface, without touching it and the sample is glued to the copper platform by silver paste. The value of $\Phi$ is kept constant $1.5\times10^{14}$ $cm^{-2}s^{-1}$ ± 0.5% using the neutral density filter method. The spectral resolution was ±5 nm. The PL was excited by the 514.5 nm line of an Ar+ ion laser, dispersed by a 0.19 TRIAX single monochromator (600 grooves/mm grating) and synchronously detected by a $N_2$-cooled InGaAs detector.

The procedure for calculating the electronic structure by means of the ETB method and the materials parameters are described in detail in [81]. The intermixing that inevitably exists in such structures was taken into account by considering a nonzero P concentration in the wire; it has been shown [81] that this method is equivalent to introducing a graded concentration profile. Since InAs/InP wires and dots are relatively flat ($H << b$), the effect of the lateral confinement on the transition energies is small [81] and was therefore neglected in our calculations. A temperature correction of 65 meV is subtracted from the calculated energies to account for the InAs band gap decrease between 0 and 300 K [82].

### 6.3.2. Results and discussion

Figure 14(a) represents the SPV spectra of the four samples in the range 0.87–1.10 eV. It is seen that the SPV amplitude increases with increasing $h\nu$ revealing a few steps superimposed on a smooth background. The exact origin of the latter is not understood very well: it could be related to deep level absorption or an Urbach tail below the InP bandgap. Though the Urbach tail is usually assumed to have exponential form, in our case the background is much better represented by a parabolic term similarly to [23]. Subtracting this term from the SPV spectrum we obtain three SPV peaks at around 0.91, 0.96 and 1.01 eV as shown in Fig. 14(b). For the sample with $d$ = 3 nm there

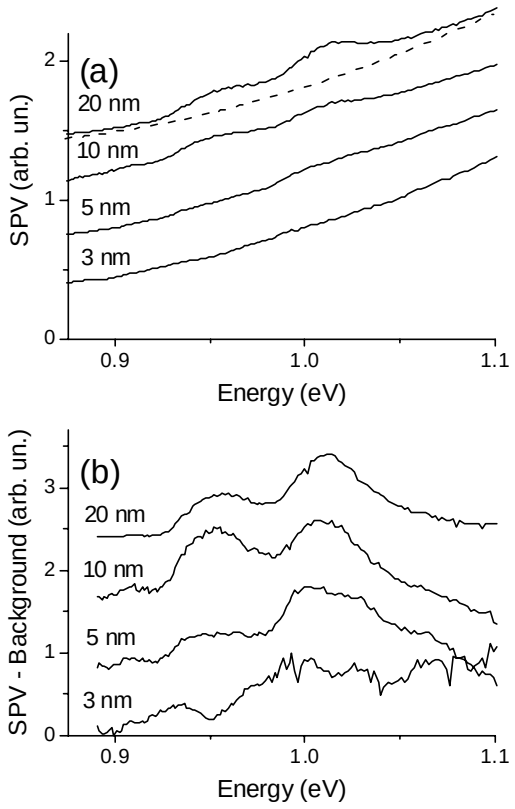


**Fig. 14.** (a) SPV spectra of samples with $d$ = 3, 5, 10, 20 nm. All curves are shifted vertically for clarity. The dashed line illustrates the background (for the sample with $d$ = 20 nm), which is subtracted and the result of this procedure applied to all samples is shown in (b).

are only two peaks at 0.93 and 0.99 eV. The SPV phase (Fig. 15) is in the $IV^{th}$ quadrant, which indicates an upward energy band bending in the SCR with respect to the bulk (see Sec. 5.1.1.). This is in accordance with the n-type residual doping of the structure and buffer layer.

The room temperature PL spectra (Fig. 16) reveal a broad band around 0.8 eV and another one at higher $h\nu$. For the samples with $d$ = 10 and 20 nm the latter band can be decomposed into three Gaussians centered at about 0.91, 0.94, and 0.98 eV. Notice that the dip at 0.89 eV is an artifact of the gratings that does not allow precise positioning of the first Gaussian – it could be at a lower energy. However, the peaks can be traced back to lower temperatures, where they appear more clearly in the PL spectra. The energy positions of these PL features are in good agreement with the optical transitions observed by SPV.

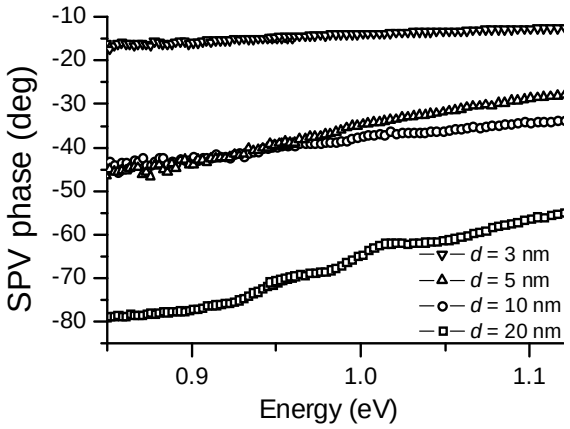


**Fig. 15.** SPV phase spectra of the four QWR samples from Fig.14.

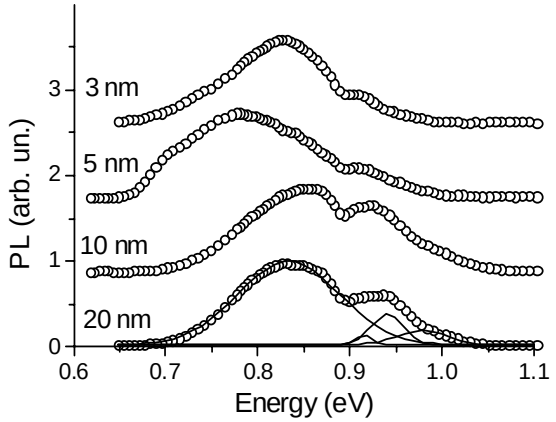


**Fig. 16.** PL spectra of the four QWR samples from Fig. 14. All curves are shifted vertically for clarity. The spectrum of the sample with $d$ = 20 nm is fitted with 4 Gaussians shown by solid lines.

Since these features are absent in the PL spectrum of bulk InP, we can ascribe them to electronic transitions arising from the QWRs. The difference between the SPV and PL peak positions represents the Stokes shift for the QWR exciton. The obtained values (20-30 meV) agree with the reported one (26 meV) for InAs/InP QWRs [80].

The SPV signal from the QWRs is due to photocarriers, which thermally escape from the InAs potential wells into the InP barriers, where they are separated by the built-in electric field of the SCR. Since the carrier escape is easier for higher energy states, the SPV peaks at higher hν are stronger. Thus, the SPV spectra complement the information obtained by PL, where the lowest energy transitions are predominantly observed.

Following the discussion in previous works on InAs/InP QWRs [26, 77, 78] we ascribe the observed PL and SPV spectral bands to excitonic transitions that take place in different QWR families having heights differing by an integer number of MLs.

Figure 17 displays the calculated transition energies as a function of the P concentration [P] in a single QWR for different values of the wire height $H$. The obtained dependences are linear. The experimental peak energies obtained by SPS are also shown with horizontal dashed lines. From the intersections between the two sets of lines the QWR heights and the P concentration are determined keeping in mind that i) $H$ should increase by a step of 1 ML and ii) [P] should remain nearly constant for the different QWR families [81]. Thus the peaks at 0.91, 0.96 and 1.01 eV are identified as originating from excitonic transitions in QWR families with $H$ = 7, 6 and 5 ML, respectively and with P concentration around 16%. These values of $H$ agree with those obtained in [26] by low-temperature PL combined with EFA calculations [77]. Taking into account the small QWR height, one can assume that the obtained value of [P], considered as homogeneous in whole the QWR, is in accordance with the

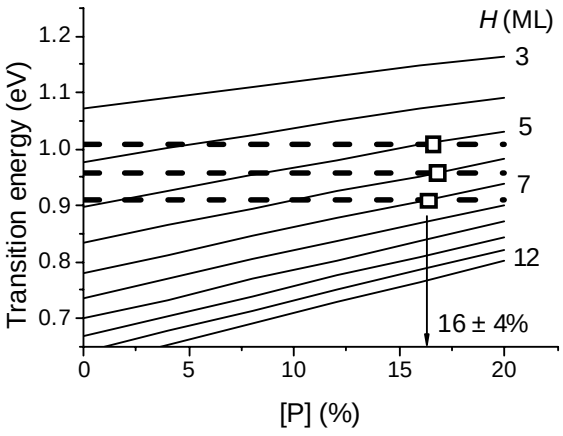


**Fig. 17.** Transition energies of a single InAsP/InP QWR as a function of the P content for wire heights from 3 to 12 MLs. The dashed lines show the SPV peak values and their relevant intersections with the calculated curves are illustrated by squares.

results from a Raman spectroscopy study of the same samples. The Raman results have shown that [P] in the QWR interface region is around 30% [27]. The error in [P] can be estimated to ± 4% and results form the uncertainty in the InAs/InP valence band offset, which is 0.3 - 0.4 eV [81] (± 2 - 3%), the experimental error in the transition energies, which is ±5 meV (±0.6%) and the effect of the strain relaxation during the QWR formation (< 1% [81]).

The lowest energy PL peak at ~0.8 eV is much broader and could account for a number of QWR families (8-12 ML high). Alternatively, this emission could originate from larger QWRs formed by the overlapping of two or more small wires, as observed by transmission electron microscopy [83] and AFM [26].

With decreasing *d* the number of thicker QWRs increases as explained in [84]. Besides, the electron coupling progressively widens the bound state energies into SL minibands, thus broadening the absorption (i.e. the SPV) spectrum. As a result the large PL peak at low hν increases at the expense of the high-energy ones, while the SPV steps become less pronounced. Also a slight red shift (~ 20 meV) of the SPV and PL spectral features is observed in Figs. 14 and 16 when *d* decreases from 20 to 3 nm. This shift is smaller than the one obtained by low-temperature PL (25-50 meV) in [26], which could be related to thermal population of nearby levels in the minibands. Due to the broad spectral shapes and the uncertainties in the peak positions in the room temperature spectra it is difficult to analyze this problem in detail.

It should be mentioned that the transitions of the *d*=3 nm sample, observed by SPV, are consistent with a lower P concentration (around 13%) than that of the other samples. This is in agreement with a decrease in the P content for thinner samples observed previously by Raman spectroscopy [27].

In summary of Sec. 6.3.: The optical absorption and emission of multi-layer InAs/InP QWRs at room temperature have been studied by SPV and PL spectroscopy, combined with structural data and ETB calculations. The existence of several QWR families with heights of 5, 6 and 7 MLs has been revealed, which supports previous findings by low-temperature PL. Further, the degree of P intermixing in the wires has been estimated to be equivalent to a constant P concentration of the order of (16±4) % and an upward direction of the energy band bending at the surface is found in accordance with the residual doping in the structure.

### 6.4. SPS of InAs/InGaAlAs/InP quantum dash-in-well laser structures

Various devices have been demonstrated based on InAs/GaAs QDs. However it is difficult to obtain emission wavelengths beyond 1.3μm with this system. As an alternative, recently there has been an increasing interest in growing self-assembled InAs dots or dashes on InP substrate to achieve the long wavelength emission [85, 86] for the optical fiber telecommunication, gas sensing, and molecular spectroscopy applications. The performance of QD lasers is further enhanced by placing the QDs within a QW; i.e., the dot-in-well structure [87]. This configuration stabilizes the QD emission wavelength and improves the injection efficiency into the quantum dots [88].

The InAs/InP QDs and QDHs emit around 1.6μm and in order to achieve the wavelength of 1.55μm, optimal for fiber telecommunication, further modification of their characteristics is necessary. Postgrowth intermixing or interdiffusion technique has been demonstrated as a simple, reliable and low-cost method to achieve monolithic photonic integration as well as to tailor the material properties in QW heterostructures [89]. Recently, intermixing technique has also been applied to quantum dot systems with promising results [90, 91]. Various QD intermixing techniques, such as impurity free vacancy disordering (IFVD) [92], nitrogen ion-implantation induced disordering (NIID) [93], and laser-induced intermixing [94] have been utilized. All these techniques include thermal annealing and the annealing temperature is critical for the interface intermixing and therefore for the obtained device properties.

For device applications using QD intermixing, the knowledge of the effect of interdiffusion is of prime importance. SPS is an alternative to the optical absorption spectroscopy, which is difficult

to perform in this case due to the small volume of the QD material. Although there are studies on QD structures using SPS (see Sec. 6.1.2.), less attention has been paid on complex nanostructures such as InAs/InGaAlAs dot-in-well structures. A pioneering SPS investigation of InAs/InGaAlAs dash-in-well (DWELL) structures grown on InP substrates has been reported in our recent papers [11, 12]. In these works we have examined the optical properties of these structures and how they are influenced by the interface intermixing, obtained by two different techniques – IFVD and NIID.

### 6.4.1. Samples intermixed by the IFVD technique

#### 6.4.1.1. Experimental details

The samples used in this study were InAs/InGaAlAs DWELL laser structures grown by MBE. The active region consists (see Fig. 18) of four undoped 5 ML thick InAs QDH layers, each one embedded within a 7.6 nm thick compressively strained $In_{0.64}Ga_{0.16}Al_{0.2}As$ QW with a 15 nm thick tensile strained $In_{0.50}Ga_{0.32}Al_{0.18}As$ quantum barrier layer. The QDH layers were grown one by one ML, each ML followed by a 5 second growth pause. A standard separate confinement heterostructure (SCH) layer consisting of a 160 nm thick undoped $In_{0.52}Ga_{0.28}Al_{0.2}As$ was grown on top of a 200 nm thick Si-doped ($1\times10^{18}cm^{-3}$) $In_{0.52}Ga_{0.48}As$ cladding layer. Both layers are lattice matched to the (100) oriented S-doped ($3\times10^{18}$ $cm^{-3}$) InP substrate. The growth was terminated after the top 160 nm thick SCH layer.

TEM measurements have revealed flat stick- or dash-like InAs islands preferentially elongated along the [0-11] direction. Their length (width) is in the range 30-60 nm (15-22 nm), while the average height is 3-4 nm. These features are also seen in the AFM images [11].

Two samples have been studied – as grown and intermixed using the IFVD technique. The IFVD procedure included rapid thermal annealing at 800 ºC in $N_2$ for 30 s. Details are given in [11].

The SPS measurements were performed with the $SnO_2$ probe isolated from the sample by a thing glass (~0.1mm). The photon flux was kept constant $2\times10^{14}$ $cm^{-2}s^{-1}$ ±2 % using the precalibrated lamp voltage method. The spectral resolution was ±5 nm. PL spectra were recorded at room temperature using a 980 nm semiconductor diode laser, a multimode optical fiber and a 0.25 m monochromator with an InGaAs photodetector [11].

#### 6.4.1.2. Results and discussion

Since the substrate and the lower cladding layer are heavily n-type doped, while the rest of the structure is nominally undoped, an upwards band bending with respect to the bulk is present in the structure. This is confirmed by the spectral behavior of the SPV phase, which increases towards -0º with increasing $h\nu$ (see Sec. 5.1.1.). Therefore, a built-in electric field is present in the

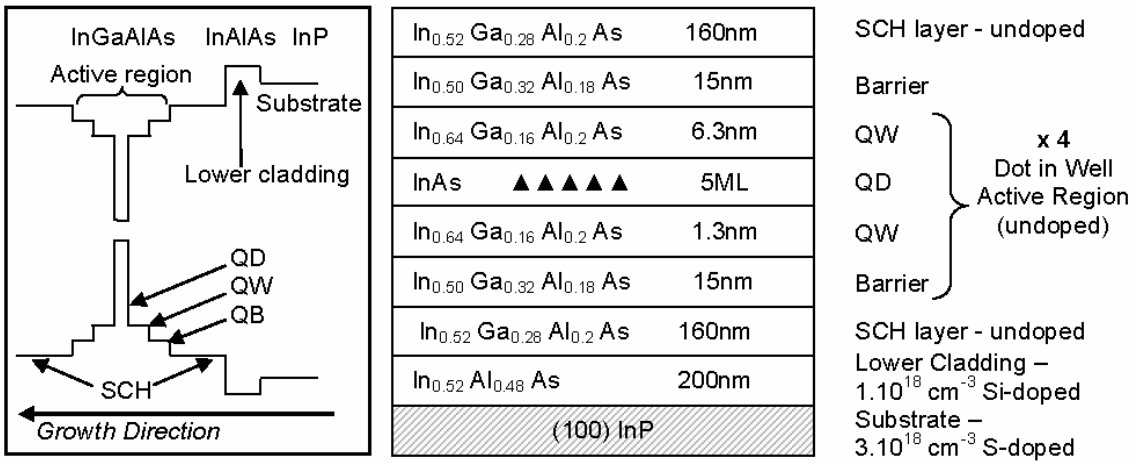


**Fig. 18.** Schematic representation of the quantum dash samples – band structure and layer sequence.

active region and SCH layers. The SPV formation processes in these complicated quantum heterostructures are discussed in detail in [11]. In brief they include electron-hole pair generation, followed by thermal or field assisted tunneling extraction of the photocarriers from the active region and their redistribution due to the built-in electric field over larger distances in the SCH and cladding layers.

Figure 19 depicts the room temperature SPV (a) and PL (b) spectra of the as grown (curves 1) and interdiffused (curves 2) DWELL samples. The SPV spectrum of the as grown sample reveals step-like features that are related to optical absorption transitions from all relevant layers in the DWELL structure: QDHs (0.734-0.796 eV), QW (0.855-0.953 eV) and SCH layer (0.968-1.097 eV), while the PL spectrum shows only a single peak corresponding to the QDH lowest energy transitions. The absence of the QW

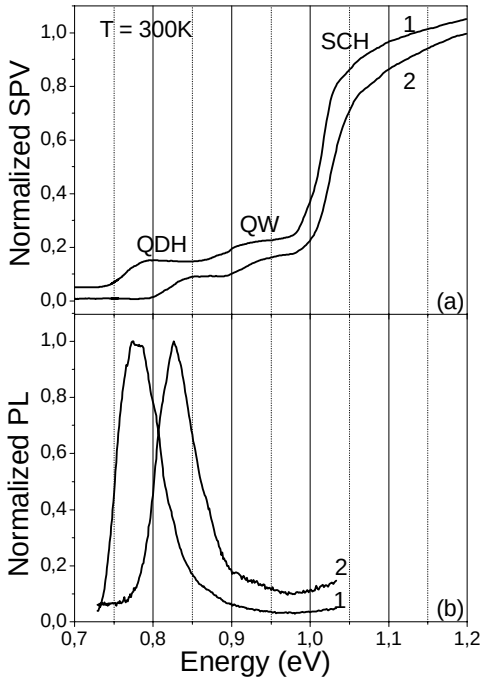


**Fig. 19.** SPV (a) and PL (b) spectra of the as grown (solid curves) and interdiffused (dashed curves) DWELL samples. Curve 1 in (a) is vertically shifted for clarity. QD stands for quantum dashes. Reprinted with permission from [Ivanov, Ts., Donchev, V., Wang, Y., Djie, H. S., and Ooi, B. S. J. Appl. Phys. 101, 114309]. Copyright [2007], American Institute of Physics.

and the SCH peaks in the PL spectrum can be explained by the relatively more effective recombination channel offered by the QDHs, which have the lowest ground states in the whole structure. The large SPV spectral range (~ 58 meV) of the QDH step is due to the inhomogeneity of their size distribution, observed also in the TEM and AFM results. The SPV spectrum in this range is composed of a series of broad Gaussians [95], corresponding to the QDH ground state as well as excited states optical transitions. It is difficult to resolve the Gaussians corresponding to different transitions, and therefore we observe a step (labeled QDH) rather than peaks in the SPV spectrum related to the QDHs. The inflection point of this step is taken here as an estimate of the QDH ground state transition energy. The obtained value (0.764 eV) is very close to the PL peak position (0.775 eV).

Curves 2 in Fig. 19 represent (a) the SPV and (b) the PL spectra of the intermixed DWELL sample, respectively. Similar to the as-grown samples, the SPV spectrum reveals step-like features that are related to all the optical absorption transitions from the QDHs, QW and SCH layer, while the PL spectrum shows only a single peak. These results clearly suggest that more features from the complex nanostructure can be retrieved from SPV rather than from PL spectroscopy. Also, it can be seen that the thermal annealing results in blue shifts of all the optical transition energies in the interdiffused structures. The shift of the QDH transition energy, determined from the inflection point of step QDH in curves 1 and 2 is approximately 52 meV [Fig. 19(a)]. The same degree of bandgap shift can be measured from the PL spectra by comparing curves 1 and 2 in Fig. 19(b). The blue shift is due to the thermally induced intermixing of group-III atoms (mainly In and Ga) between the InAs QDHs and the surrounding InGaAlAs [92]. The intermixing modifies the compositional profile from an abrupt interface to a graded one resulting in an interfacial graded potential. As a consequence the potential increases in the InAs QDH region while it decreases in the surrounding InGaAlAs barrier, i.e. the QW region. The first effect pushes the QDH bound state energy levels up, while the second one pushes them down. Since the wave

functions of the QDH ground states are localized predominantly in the central part of the QDHs, the first effect is stronger. Thus, their energies and therefore the optical transition energy increase, which leads to the observed blue shift of the SPV and PL spectra.

The blue shift of the QW transition energy, as determined from the inflection point of step QW in curves 1 and 2, in Fig. 19(a) is around 27 meV. There are two interfacial effects that influence the potential in the QW: i) the intermixing of the interfaces QW/QDHs decreases the potential in the QW layer; ii) the intermixing of the interfaces QW/quantum barrier increases the potential in the QW layer. As the QDH volume is smaller as compared to those of the QW and of the quantum barrier, the second effect is stronger, which results in a blue shift of the QW bound state energy levels and correspondingly to the QW optical transition after annealing. The shift value is smaller than that of the QDH transition. This is due to the larger surface-to-volume ratio of the QDHs, which is more influenced by the intermixing induced changes of the interface potential. The blue shift is further reduced with increasing the volume of the corresponding layer: The SCH transition energy (step SCH) only shifts by ~7 meV, while the InP substrate transition energy is unchanged after annealing.

Figure 19 also suggests that the intermixing improves the homogeneity of the QDH size distribution. Indeed the step QDH in the SPV spectrum of the annealed sample extends in a narrower spectral range (0.795 – 0.850 eV) than that of the as-grown one, with a difference of approximately 11 % [compare curves 1 and 2 in Fig. 19(a)]. The improvement of the QDH size homogeneity is also evidenced by the PL linewidth narrowing. The full width at half maximum of curves 1 and 2 in Fig. 19(b), evaluated after subtracting the noise level are 62 and 56 meV, respectively. The narrowing (~10%) is almost the same as that observed in the SPV spectra.

### 6.4.2. Samples intermixed by the NIID technique

#### 6.4.2.1. Experimental details

The investigated samples are partial InAs/InGaAlAs DWELL laser structures grown by MBE, similar to those from the previous section. The only distinction is the absence of the upper SCH layer. The applied NIID intermixing procedure is described in details in [12]. The samples were first bombarded with N ions and then annealed at 700°C for 2 min with no annealing cap to avoid any possible IFVD effect. For comparison purposes we have studied also a control sample annealed at the same conditions, but without ion implantation, as well as an as-grown sample.

The SPS and PL measurements were performed as described in the previous section with the only distinction of the 532 nm diode pumped solid state laser (1.5 $kWcm^{-2}$) used in the PL spectroscopy.

#### 6.4.2.2. Results and discussion

Figure 20 summarizes the SPV and PL results on all the three samples. The SPV spectra reveal step-like features, which energy ranges coincide very well with the positions of the corresponding PL peaks. As explained in Sec. 6.4.1.2, due to the inhomogeneous QDH size distribution, each SPV steps is composed of a series of broad Gaussians [95], corresponding to the QDH ground state as well as excited states optical transitions. The energy position of the ground states transition is

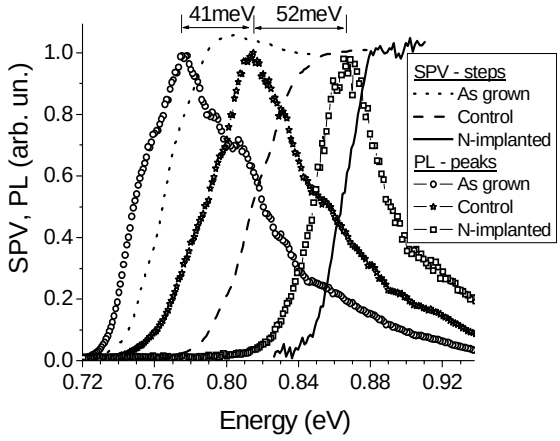


**Fig. 20.** SPV (lines) and PL (lines & symbols) of as grown, control and N-implanted samples. Reprinted with permission from [Ivanov, Ts., Donchev, V., Bachev, K., Ding, Y-H., Wang, Y., Djie, H. S., and Ooi, B. S. J. Phys.: Conf. Ser., 113**,** 012033, (2008)] Copyright IOP Publishing Ltd.

in the range of the steep slope of the SPV step, where a weak shoulder can be seen (for the as grown and control samples). It can be determined more precisely from the position of the corresponding PL peak, which has been proven to reveal the ground state position (the peak does not shift with decreasing the excitation density). The PL spectrum of the as-grown and the control samples shows also a few excited state transitions, whose energies are situated in the region corresponding to the flat part of the SPV step.

Figure 20 shows that there is a total blue shift as large as 93 meV (176nm) between the as grown and the N-implanted sample, calculated from the SPV step and PL peak positions. It is explained as follows. The N ion implantation introduces vacancies and interstitial defects in the sample, with a peak defect density centered at 0.8μm below the active region of the structure [12]. During the annealing these defects effectively diffuse towards the active region to enhance the thermally induced intermixing [91]. The intermixing of group-III atoms (mainly In and Ga) between the InAs QDHs and the surrounding InGaAlAs QW modifies the compositional profile from an abrupt interface to a graded one, resulting in an interfacial graded potential. This leads to a blue shift of the bound states and the corresponding transition energies, as explained in Sec. 6.4.1.2 and [11]. For comparison, the blue shift of the control sample is only 41meV (80nm) because the intermixing in this case is simply due to grown-in defects diffusion during the annealing process. The net effect of N implantation is seen from the comparison between the spectra of the control and the N-implanted samples – the differential bandgap shift is also significant, namely 52 meV (96nm), which proves again the role of the implantation induced defects in the intermixing process. It should be noted that the same amount of blue shift (52meV) has been obtained by means of the IFVD technique, but employing a 100°C higher annealing temperature (see Sec. 6.4.1.2).

The N implantation also leads to step narrowing in the SPV spectrum (approximately 50%) as well as to PL line width reduction (approximately 40%) as can be seen from the comparison of the spectra of the control and the N-implanted samples on Fig. 20. This is due to the improved homogeneity of the QDH size distribution during the intermixing, which is in accordance with the results in [91]. Another possible reason for this narrowing could be the fact that after the intermixing the QDH bound states become closer in energy (the potential well of the QDH becomes shallower). This does not allow to resolve the Gaussians corresponding to the ground and excited states transitions, which results in a smoother SPV step of the N-implanted sample revealing no shoulders (contrary to the SPV spectra of the other two samples).

In summary of Sec. 6.4.: Room temperature SPV and PL spectroscopy have been used to characterize inter-band optical transitions in as-grown and interdiffused InAs/InGaAlAs DWELL structures. Compared with PL, the SPS is more advantageous since SPV signals can be detected from all relevant layers in the DWELL structure including the QDHs, QW, and SCH layers, while only the QDHs give PL signal. The blue shift of the inter-band optical transition energies resulting from the group-III intermixing in the interdiffused structures has also been revealed by SPS and the results have been confirmed by the PL measurements. Employing the NIID technique has resulted in larger differential blue shift as compared to the IFVD technique, even using lower annealing temperatures, which shows the potential of the former for bandgap tuning of monolithic photonic devices.

### 6.5. SPS of multi-layer self-assembled InP/GaAs quantum dots

The InP/GaAs quantum dots are type II heterostructures, where the electron is confined in the InP material while the hole remains in the GaAs layer around the QDs, due to the Coulomb attraction toward the electron [34, 96]. It is expected that the spatial separation of the electron and the hole will lead to small overlap of their wave functions, resulting in relatively long carrier lifetimes [97]. Due to these properties and their near-infrared (~0.95 μm) optical transition energies, InP/GaAs QDs are potential candidates for optical memories and optical communication devices.

These type II QD heterostructures are more complex systems as compared to type I QDs,

because of the different possibilities for hole wave function distribution around the QD, which is very sensitive to the QD geometry [98]. The study of multi-layer type II QDs is further complicated, because of the structural and electronic couplings between dots adjacent along the growth direction, which depends on the spacer layer parameters. So far the published works devoted to the optical properties of InP/GaAs QDs are mainly based on PL investigations [33, 34, 98, 99]. Few results are available in the literature concerning optical absorption measurements of type II QD systems [100], probably due to the relative novelty of the research field and the general difficulties related to the optical absorption spectroscopy in nanostructures. As for the nanostructures considered in the previous sections, in this case again the SPS is a promising alternative to the optical absorption.

In this section we describe our SPS study of the optical properties of multi-layer self-assembled InP/GaAs QDs, combined with PL measurements.

### 6.5.1. Experimental details

The self-assembled InP/GaAs QDs were grown by the Stranski-Krastanov mode in a chemical beam epitaxy (CBE) system. The growth details were similar to the ones given in [34] for single layer QD structures. The present sample contains 10 periods of InP/GaAs QDs layers separated by 5 nm thick GaAs spacer layers. The top QD layer is left uncovered in order to perform AFM measurements. The structure is grown on a 300 nm GaAs buffer layer deposited on a (001) oriented SI GaAs substrate. A schematic of the sample structure is shown in Fig. 21. The CBE grown multilayer structure and GaAs buffer have a p-type residual doping of around $10^{16}$cm$^{-3}$, originating mainly from carbon, which is a commonly present shallow acceptor in the CBE growth process.

The SPS measurements were performed employing the $SnO_2$ probe in soft contact mode. The photon flux was kept constant $2\times10^{14}$ cm$^{-2}$s$^{-1}$ ± 2 % using the precalibrated lamp voltage method. The spectral resolution was ±5 nm. The SPV phase was measured between 0° and 360°. PL measurements at 10 K were also performed using a 200 mW diode laser for excitation with 532 nm light, a SPEX single monochromator (1200gr/mm) and a Ge detector connected to a Lock-in amplifier.

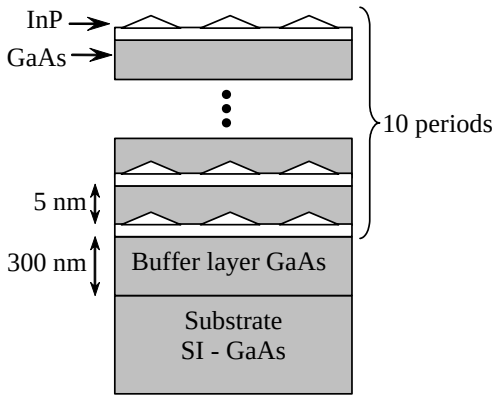


**Fig. 21.** Layer sequence in the sample.

### 6.5.2. Results and discussions

AFM measurements, performed on a 1x1μm$^2$ area of the top layer, have revealed a dot density of $3.5\times10^{10}$ cm$^{-2}$. The QD height (*H*) varies from ~1.5 to more than 7 nm with an average value of (3.2±0.9) nm and the corresponding QD radius (*R*) is between ~12 and ~24 nm with an average value of (18±3) nm. Note that the larger dots in the inner layers should coalesce, forming quantum posts [101], because their height exceeds the spacer thickness.

A typical SPV amplitude spectrum of the QD sample at room temperature is presented on Fig. 22 with empty squares. It can be divided into two parts: a low-energy region for photon energies $h\nu$ < 1.35 eV and a high-energy one for $h\nu$ > 1.35 eV. We first discuss the low-energy region. It includes two major bumps in the ranges 1.05 - 1.15 eV and 1.25 – 1.35 eV, respectively. There are a couple of less pronounced shoulders between them. All the features depicted above can be better seen in the derivative of the SPV amplitude spectrum as peaks corresponding to their inflection points (see inset in Fig. 22). Accordingly, two principal peaks can be seen in the energy ranges of the two major spectral bumps.

We could not detect any PL at room temperature in the sample. That is why, in order to compare the SPV results with PL ones, we have used the

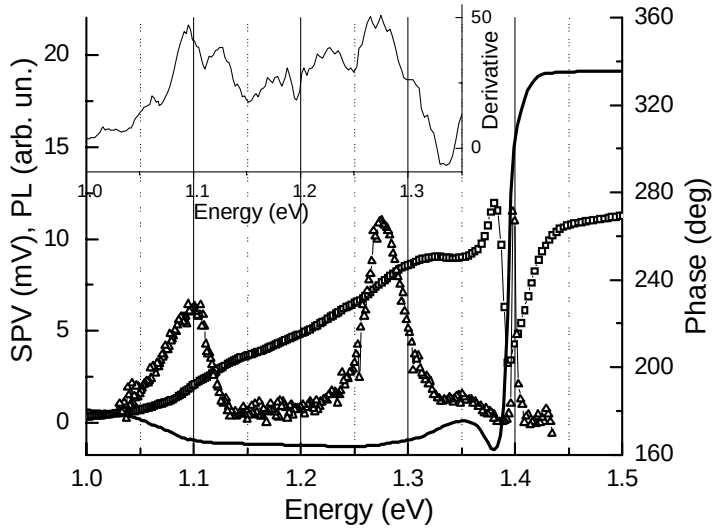


**Fig. 22**. Room temperature SPV amplitude (squares) and phase (solid line) spectra, 10 K PL (triangles) spectrum (with energy correction to 300K, see the text) and derivative (inset) of the SPV amplitude spectrum.

PL spectrum of the sample measured at 10 K. For the purposes of this comparison the PL spectrum is translated to lower energies. Although the red shifts of the QD transitions and the GaAs bandgap occurring upon increasing the temperatures may be slightly different, as a first approximation we have shifted the PL spectrum in accordance with the temperature dependence of the GaAs bandgap energy (96 meV change between 10 and 300 K [67]). It is represented by triangles in Fig. 22 and reveals two broad peaks centred at 1.10 and 1.28 eV, respectively. It should be noted that the PL peak positions in type II heterostructures depends on the excitation density [33, 102], which is different in our SPV and PL experiments. Since it was not possible to detect any PL with an excitation density as low as that used in the SPV experiment, we have applied 5 $Wcm^{-2}$, which is one of the lowest possible excitation densities that give a reasonable PL signal in the sample. The investigation of the temperature and excitation density dependencies of the PL spectra goes beyond the scope of this study. Nevertheless we have checked that the PL spectral shape does not change essentially with decreasing the excitation density and increasing the temperature. This allows comparing the SPV and PL spectra presented here. Figure 22 shows a good correspondence between them in the lower energy region – the energy positions of the PL peaks are close to the ones of the two major SPV bumps. This result allows us to conclude that the SPV bumps and PL peaks are due to optical transitions between the same energy states.

Further on, in order to assess the possible influence of the SPV generated in the substrate, we have measured a SPV spectrum of the bare substrate, shown in Fig. 23. It is seen that in the spectral range 1.0 - 1.35 eV, where the signal from the QD structure is expected, the SPV is very low and exhibits no distinct spectral features. The comparison of the SPV spectra of the QD sample and of the substrate implies that the features observed in Fig. 22 for $h\nu < 1.35$ eV originate from the InP/GaAs QD layers.

The presence of two well separated bands in both absorption (SPV) and emission spectra of the investigated multi-layer InP/GaAs QD sample is an intriguing result, taking into account that in previous studies on single layer InP/GaAs QDs the emission bands of the QDs and the wetting layer (WL) were overlapping in one single band [34].

We attribute the band around 1.11 eV to electronic transitions from the valence band (VB) states in the GaAs spacer layers to the conduction band (CB) states in the InP QDs. The band at 1.27 eV is tentatively ascribed to similar transitions, but involving the CB states of the WL instead of

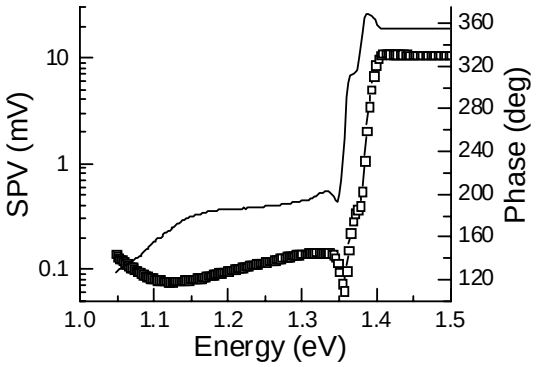


**Fig. 23.** SPV amplitude (empty squares) and phase (solid curve) spectra of the SI GaAs substrate.

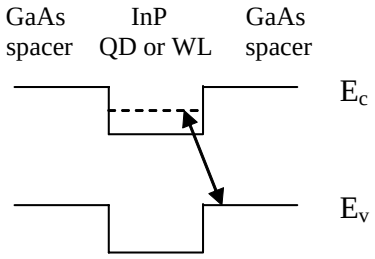


**Fig. 24.** Schematics of the energy band line-up and electronic transitions in one period of the multi-layer InP/GaAs QD structure. The dashed line marks the energy level of the electron bound state in InP.

the QDs. This attribution is in accordance with the electronic structure calculations, performed by means of a simple one-band EFA model and the QD sizes, obtained by AFM. The WL transition energies were calculated considering coupled InP layers, each with a constant thickness $d_{WL}$=2 nm. Since the InP/GaAs QDs are relatively flat ($H << R$), the effect of the lateral confinement on the transition energies is small and was therefore neglected in our calculations. Thus, the multi-layer QDs are considered as multi-quantum wells with CB offset of 300 meV [98] and a width equal to $H+d_{WL}$. The electron effective masses are taken $0.079m_0$ and $0.065m_0$ for InP and GaAs, respectively [67]. For simplicity the weak confinement of the heavy holes is neglected and the hole level is always taken to coincide with the top of the GaAs VB as illustrated in Fig. 24. The results obtained for different values of the QD height are summarized in Table 2 together with the experimental transition energies.

It is seen from Table 2 that there is a reasonable agreement between the experimental energy of the high-energy band and the calculated one for the WL. These energies are a bit lower than the ones observed for WL emission transitions in single layer InP/GaAs QDs [34, 103] (~1.35 eV after the 96 meV temperature correction), which is consistent with the expected coupling effect for the multi-layers.

As expected, the energy position of the low energy band best fits with the value, calculated for the highest QDs ($H$ equal to the spacer thickness), which coalesce in quantum posts. The large size of the quantum posts accounts for the relatively low energy of this band as compared to the emission energy in single-layer capped QDs [34, 102] (1.28 – 1.30 eV, after the 96 meV temperature correction). In this case the electron confinement energy, obtained in our model is very small (1 meV). In the real case it should not be very different from this value, because of the small lateral confinement (large QD diameter). So, for such quantum posts the electron and hole energy levels are close to the bulk InP CB minimum and bulk GaAs VB maximum, respectively and the transition energy directly reflects the CB offset used in our calculation (300 meV). It should be noted that the observed correspondence between calculated and experimental transition energies described above is quite satisfactory taking into account the uncertainty in the band-offset value, as well as the fact that the effects of strain and interface intermixing are not included in our simple model. Photon absorption in smaller dots (see Table 2) contributes to the increasing SPV signal for $h\nu > 1.10$ eV up to the onset of the WL transitions (see Fig. 22).

The observation of steps and bumps instead of peaks in the SPV amplitude spectrum can be explained by transitions between closely spaced ground and excited state energy levels in the structure, which are inhomogeneously broadened, due to the dot size distribution. On the one hand the relatively thin spacers (5 nm) between the QD layers favour the electron wave function delocalisation along the stack direction [104], which widens the electron bound state energies into SL minibands. On the other hand, the strain distribution in the GaAs spacer layers around the

**Table 2.** Experimental transitions energies (in eV) of the low- and high-energy bands in the SPV and PL spectra of the InP/GaAs QD samples, compared to calculation results (see text).

| $H$ (nm) | $H+d_{WL}$ (nm) | Low-energy band | | High-energy band | |
|---|---|---|---|---|---|
| | | Calculated QD energy | Experiment SPV (PL) | Calculated WL energy | Experiment SPV (PL) |
| 1.5 | 3.5 | 1.24 | 1.05 - 1.15 (1.10) | 1.31 | 1.25 – 1.35 (1.28) |
| 3.2 | 5.2 | 1.18 | | | |
| 3.7 | 5.7 | 1.17 | | | |
| 4.2 | 6.2 | 1.15 | | | |
| 5.0 | 7.0 | 1.12 | | | |

dots splits the heavy and light hole bands which could result in a series of excited states for holes. All these effects will broaden the absorption (SPV) spectrum.

As emphasized in our previous works [9, 10] the SPV amplitude should be analyzed together with the SPV phase spectrum in order to obtain a correct understanding of the experimental data. In particular the SPV phase gives information about the mechanisms, via which the photogenerated carriers are separated in space in order to produce a SPV signal.

In order to clarify the mechanisms, via which the photogenerated carriers are separated in space to produce a SPV signal we analyse also the SPV phase spectrum, represented by solid line in Fig. 22. In the spectral range, where the QDs start to absorb ($h\nu$ ~1.05 eV) the SPV amplitude increases, while the phase acquires a value close to 160° and remains nearly constant over the whole range of QD and WL absorption. This means that the holes generated via the QD transitions move toward the bulk [4, 10], which can be due to drift in the SCR and/or diffusion, which is more efficient than that of the electrons.

Let us first consider the SPV contribution of the carrier drift in the SCR. From the p-type residual doping of the multilayer structure and buffer layer it is expected that the energy bands at the surface are bent downward with respect to the bulk, which is typical for p-type semiconductors. The built-in electric field of the SCR induces a hole drift towards the bulk and electron drift towards the surface, which is in accordance with the observed SPV phase value.

Let us then consider the SPV contribution of the carrier diffusion. In order to leave the QD structure and move towards the substrate, the electrons from the InP QDs have to overcome the barrier of the GaAs buffer layer and the built-in electric field of the SCR. In addition, the QDs in the first layer are usually smaller than the others [99], which represents another barrier for electrons. In the same time the holes, situated in the GaAs spacer layers, can migrate to the lower energy regions aside the dots where they have much more freedom to move vertically towards the bulk (as compared to the electrons) because the InP barriers of the WL are very thin and no additional barrier between the structure and the GaAs buffer layer exists. Besides, the hole diffusion towards the bulk has the same direction as their drift in the SCR electric field.

Thus, the holes photogenerated in the QPs, move predominantly toward the bulk via drift and diffusion, while the corresponding photogenerated electrons predominantly drift towards the surface. As the QD structure is very thin (~ 65 nm), the holes travel much longer distances (including part of the GaAs buffer layer) than the electrons. We believe that this is the main mechanism that separates the photocarriers over longer distances and gives rise to the SPV signal in the lower energy spectral region with a phase close to 160°.

The inclusion of the WL transition around 1.25 eV increases the SPV amplitude, but the phase remains practically the same, which indicates that the QD and the WL signals have the same phase retardation. This result is expected since, as explained above, in both cases the signal

is obtained mainly from the holes, photogenerated in the GaAs spacers and their movement towards the bulk, which is realized practically in the same way.

Below we discuss the high-energy region ($h\nu > 1.35$eV) of the SPV spectrum (Fig. 22) The amplitude increases above 1.35 eV, but its rise is interrupted at 1.38 eV by a sharp decrease, followed by a deep minimum at 1.39 eV and finally by a nearly constant value above 1.44 eV. The phase in this range first exhibits a smooth change from ~180° towards 160°, but at 1.38eV its run reverses direction and a drastic jump of nearly 180° occurs, followed by a constant value of ~340° for $h\nu$ above the GaAs band gap energy. The phase jump corresponds in energy to the deep minimum in the amplitude spectrum. Similar spectral behaviour of the SPV amplitude and phase in the near-bandgap spectral range is observed also in the spectra of the SI GaAs substrate (Fig. 23). Therefore it is connected with the substrate contribution to the SPV signal in this range. To understand and explain the nature of the observed spectral peculiarities we take into account that in SI GaAs the energy bands are practically flat and the dominant processes that give rise to SPV signal are the Dember voltage effect in the bulk as well as the different carriers emission and recombination rates of the defect states in the bandgap [4, 75]. The Dember effect relies on the difference in the carrier mobilities and since the electrons diffuse faster than holes, the SPV phase is close to 360°. Electron emission from a defect level (trapped hole) will results in a phase close to 360°, too, while hole emission (trapped electron) – in a phase close to 180°.

The discussion of the high-energy region is carried out with the help of the vector model for the SPV signal. (see Sec. 5.2. and [9]). The initial amplitude increase in the range 1.35-1.38 eV accompanied with a small phase change in the II$^{nd}$ quadrant (from ~180° to ~160°) indicates the appearance of a process with phase in the same quadrant. It can be ascribed to electron transitions between the VB and shallow traps near the CB (trapped electron), which provide predominantly free holes. For higher energies the amplitude minimum (1.39 eV) and the ~180° phase jump indicate the inclusion of a new process opposite in phase to the process depicted above (i.e. its phase is close to 360°). Therefore it results in electrons (rather than holes) moving towards the bulk [9, 10]. The addition of the two types of processes is schematically illustrated in Fig. 25 as the addition of two vectors: 1- corresponding to the processes generating free holes, and 2 - to the processes generating free electrons. These vectors form obtuse angle close to 180$^o$. Vector 2 increases with increasing $h\nu$ and for $h\nu$ = 1.39 eV its magnitude becomes comparable to that of vector1.

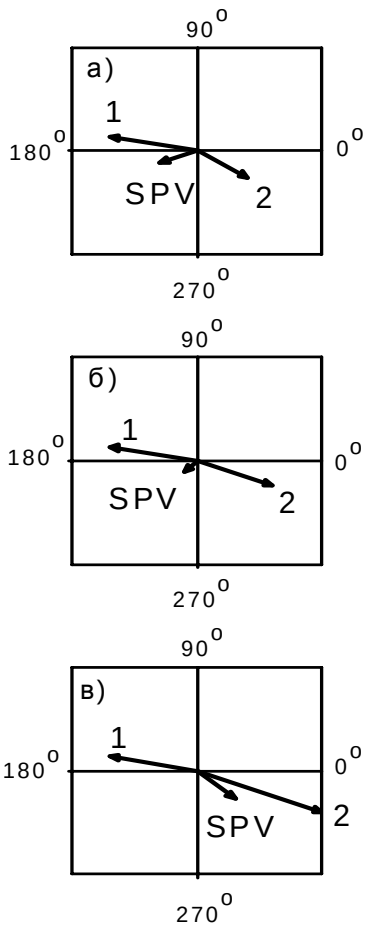


**Fig. 25.** The arising and the increase of vector 2 (in the IV$^{th}$ quadrant), which is added to the constant vector 1 (in the II$^{nd}$ quadrant) leads to non-monotonic behaviour of the overall SPV vector amplitude: initially it decreases [(a) - (b)], reaches a minimum (b) and then increases again [(b) - (c)]. In the same time the phase of the SPV vector continuously rotates counter clockwise towards 360$^o$.

Then the summation of 1 and 2 leads to a small resultant SPV vector [see Fig. 25(b)], i.e. small amplitude of the total SPV signal. We believe that first electron transitions from shallow acceptors to the CB set in providing free electrons (trapped holes) and therefore start to change the phase anticlockwise towards 360° as well as to decrease the total SPV amplitude. Further, the band to band free carrier generation in the GaAs substrate begins, which is a strong process with a phase also close to 360° due to the Dember effect. It overpowers the previous processes and dominates after $h\nu$ = 1.42 eV leading again to large SPV amplitude. The above described succession of SPV generation processes explains the deep minimum in the amplitude spectrum, as well as the phase jump at 1.39 eV. Therefore the SPV peak at 1.38 eV is an artifact. This result clearly demonstrates our conclusion that the simultaneous analysis of the amplitude and phase SPV spectra is necessary in order to retrieve correct information for the physical nature of the observed spectral features (see Sec.5.1.).

The energy position of the shallow acceptor-to-CB transitions can be seen as a sharp peak at 1.40 eV in the PL spectrum.

The discussion of the high-energy region of the SPV spectrum is in agreement with the analysis of the SPV results in bulk SI GaAs samples presented by other authors [4].

In conclusion of this section, SPS measurements have revealed the optical transitions in multi-layer InP/GaAs QD structures, related to the QDs and the WL as two well separated spectral bands, in good correspondence with two peaks observed in the PL spectrum. Their energy positions are lower as compared to those in single layer InP/GaAs QDs. These results have been explained by electronic coupling effects in the multi-layers, as well as by vertical coalescence of large QDs, leading to quantum posts formation. The mechanisms of photocarrier separation in the space are discussed and it is concluded that the principal one is the predominant hole drift and diffusion from the QD structure towards the substrate bulk. The SI GaAs substrate absorption via band-to-band transitions, as well as transitions between shallow levels and the bands has been revealed in the SPV spectra for $h\nu > 1.35$ eV. The obtained results contribute to better understand the optical properties of multi-layer InP/GaAs QDs in view of their optimization for device applications.

## 7. CONCLUSION

We have presented a review paper devoted to the SPS. After a brief review of the basic principle of the SPS and the experimental methods for its realization we have described our SPS experimental set-up, which works in MIS operation mode and is fully automated. The latter allows contactless and non-destructive measurements in wide spectral and temperature ranges. Besides, an overview of the SPS studies of different nanostructures performed by other authors in the last decade is given. To our knowledge no complete description of these studies has been published until now.

Further on, some advances in the SPS, which have been the subject of our recent research efforts in this field, are presented. First, it is shown that the simultaneous investigation of both amplitude and phase SPV spectra is necessary in order to obtain correct understanding of the experimental data. In this connection we propose two original approaches, concerning the application of the SPV phase spectral measurements for characterization of bulk semiconductors and nanostructures: i) We have shown that the sign of the bandgap-related knee in the SPV phase spectrum depends on the direction of the surface band bending (up or down) and hence it can be used as a handy tool for determining the semiconductor type (n or p). It is shown that the proposed approach can be applied also to multilayered structures, containing buried interfaces in order to obtain the band bending direction in the sample region, where the light is absorbed; ii) We have demonstrated that in the non-linear recombination case the SPV phase spectrum reflects the features of the optical absorption coefficient spectrum, and therefore gives information on the optical transitions, which is similar to the one retrieved from the SPV amplitude and PL spectra.

Second, another original approach is proposed, which allows an easier and reliable analysis of the SPV amplitude and phase spectral behavior. It consists in developing of a vector model, in which the SPV signal is represented by a radial vector, containing all the information given by the SPV

amplitude and phase spectra. The model is especially useful when more than one SPV generation process occurs during the run of the spectrum.

Further, we have presented the results of our pioneering studies of some new complicated nanostructures with graded interfaces including AlAs/GaAs superlattices with GaAs embedded quantum wells, InAs/InGaAlAs quantum dashes-in-well laser structures, multilayer InAs/InP quantum wires, and multilayer InP/GaAs type II quantum dots. The amplitude and phase SPV spectra in all the cases are analyzed and explained simultaneously using the vector model for the SPV signal. The comparison of the SPS results with those obtained by PL spectroscopy and by electronic structure calculations in frames of the envelope function approximation and the empirical tight binding methods has shown a very good agreement. Thus, important information about the bound electronic states, the excitonic optical transitions, and the interface grading effects in the investigated systems has been obtained.

This review highlights the potential of the SPS as an advanced method for investigation of the electronic and optical properties of complex nanostructures at room temperature. It is shown also that in many cases the SPS is a valuable alternative of the optical absorption spectroscopy and is more informative than the PL spectroscopy.

Finally, the results presented here could be useful for the quickly developing field of the nanophysics, as well as for the fabrication of unique devices, designed for different applications.

## ACKNOWLEDGEMETS

Financial support from the Bulgarian National Science Fund, (contracts D01-463/12.07.06 and VUF-203/06), the Sofia University Research Fund and the Alexander von Humboldt Foundation is acknowledged. The authors are thankful to D. Martin (EFPL, Switzerland) for supplying the EQW samples, to A. Cros and T. Angelova (University of Valencia, Spain) for the QWR samples and their PL measurements, to B. S. Ooi, H. S. Djie and Y. Wang (Lehigh University, USA) for the QDH samples and their PL spectra, and to F. Iikawa and M. A. Cotta (UNICAMP, Brazil) for the QD samples and their AFM measurements. All the people mentioned above are acknowledged for helpful discussions, too. One of the authors (V.D.) is thankful to the FAPESP foundation (Brazil) for the research fellowship on InP/GaAs QDs. One of the authors (K.G.) acknowledges the Alexander von Humboldt Foundation for the research fellowship on SPV phenomena.

## REFERENCES

1. Kronik, L. and Shapira, Y. 1999, Surf. Sci. Rep., 37, 1-206.
2. Kronik, L. and Shapira, Y. 2001, Surf. Interface Anal., 31, 954-965.
3. Schroder, D. K. 2001, Meas. Sci. Tech., 12, R16-R31.
4. Sharma, T. K., Kumar, S., and Rustagi, K. C. 2002, J. Appl. Phys., 92, 5959-5965.
5. Chan, C. H., Lee, C. H., Huang, S. Y., Wang, J. S., and Lin, H. H. 2007, J. Appl. Phys., 101, 103102.
6. Bhattacharyya, J., Ghosh, S., Malzer, S., Dohler, G. H., and Arora, B. M. 2005, Appl. Phys. Lett., 87, 212101.
7. Donchev, V., Kirilov, K., Ivanov, T., and Germanova, K. 2007, Journal of App. Phys., 101, 124305.
8. Ivanov, T., Donchev, V., Kirilov, K., and Germanova, K. 2007, J. Optoel. & Adv. Mat., 9, 190-193.
9. Ivanov, T., Donchev, V., Germanova, K., and Kirilov, K. 2009, J. Phys. D: App. Phys., 42, 135302.
10. Donchev, V., Kirilov, K., Ivanov, T., and Germanova, K. 2006, Mat. Sci. & Eng. B, 129, 186-192.
11. Ivanov, T., Donchev, V., Wang, Y., Djie, H. S., and Ooi, B. S. 2007, J. Appl. Phys., 101, 114309.
12. Ivanov, T., Donchev, V., Bachev, K., Ding, Y. -H., Wang, Y., Djie, H. S., and Ooi, B. S. 2008, J. Phys. Conf. Series, 113, 012033.
13. Donchev, V., Ivanov, T., Angelova, T., Cros, A., Cantarero, A., Shtinkov, N., Borisov, K., Fuster, D., González, Y., and González, L. 2010, J. Phys.: Conf. Series, 210 (2010) 012041.
14. Ivanov, T., Donchev, V., Germanova, K., Gomes, P. F., Iikawa, F., Brasil, M. J. S. P., Chiaramonte, T., and Cotta, M. A. (Sec.6.5. in this review).

15. Touskova, J., Samochin, E., Tousek, J., Oswald, J., Hulicius, E., Pangrac, J., Melichar, K., and Simecek, T. 2002, J. Appl. Phys., 91, 10103.
16. Liang, J. S., Wang, S. D., Huang, Y. S., Tien, C. W., Chang, Y. M., Chen, C. W., Li, N. Y., Tiong, K. K., and Polak, F. H. 2003, J. Phys. Cond. Matt., 15, 55-66.
17. Datta, S., Arora, B. M., and Kumar, S. 2000, Phys. Rev. B, 62, 13604.
18. Dumitras, G., Riechert, H., Porteanu, H., and Koch, F. 2002, Phys. Rev. B., 66, 205324.
19. Sharma, T. K., Porwal, S., Kumar, R., and Kumar, S. 2002, Rev. Sci. Instrum., 73, 1835.
20. Zhang, Y., Xie, T., Jiang, T., Wei, X., Pang, S., Wang, X., and Wang, D. 2009, Nanotechnology, 20, 155707.
21. Fox, N. E., Sharma, T. K., Sweeney, S. J., and Hosea, T. J. C. 2009, Phys. Status Solidi A, 206, 796-802.
22. Malikova, L., Holden, T., Perez-Paz, M. N., Munoz, M., and Tamargo, M. C. 2009, Appl. Phys. Lett., 94, 102109.
23. Sharma, T. K., Hosea, T. J. C., Sweeney, S. J., and Tang, X. 2008, J. Appl. Phys., 104, 083109.
24. Chan, C. H., Chen, H. S., Kao, C. W., Hsu, H. P., Huang, Y. S., and Wang, J. S. 2006, J. Appl. Phys., 100, 064301.
25. Wang, P., Kurayama, S., Fukuyama, A., Akashi, Y., and Ikari, T. 2007, Jap. J. Appl. Phys., 46, 6857-6859.
26. Fuster, D., Martínez-Pastor, J., González, L., and González, Y. 2006, J. Phys. D: Appl. Phys., 39, 4940-4947.
27. Angelova, T., Cros, A., Cantarero, A., Fuster, D., González, Y., and González, L. 2008, J. Appl. Phys., 104, 033523.
28. Sek, G., Podemski, P., Musial, A., Misiewicz, J., Hein, S., Hoefling, S., and Forchel, A. 2009, J. Appl. Phys., 105, 086104.
29. Djie, H. S., Dimas, C. E., and Ooi, B. S. 2006, IEEE Photon. Tech. Lett., 18, 1747-1749.
30. Djie, H. S., Wang, Y., Ding, Y.-H., Wang, D.-N., Hwang, J. C. M., Fang, X.-M., Wu, Y., Fastenau, J., Liu, A. W. K., Dang, G. T., Chang, W. H., and Ooi, B. S. 2008, IEEE Journal of selected topics in quantum electronics, 14, 1239-1249.
31. Bimberg, D., Grundmann, M., and Ledentsov, N. N. 1998, Quantum Dot Hetereostructures, Wiley, Chichester, 1.
32. Moskalenko, E. S., Karlson, F. K., Donchev, V. T., Holtz, O., Monemar, B., Schoenfeld, W. V., and Petroff, P. M. 2005, Nano Lett., 5, 2117-2122.
33. Wang, B., and Chua, S.-J. 2001, Appl. Phys. Lett., 78, 628.
34. Godoy, M. P. F. d., Nakaema, M. K. K., Iikawa, F., Brasil, M. J. S. P., Lopes, J. M. J., Bortoleto, J. R. R., Cotta, M. A., Magalhaes-Paniago, R., Morschbacher, M. J., and Fichtner, P. F. P. 2007, J. Appl. Phys., 101, 073508.
35. Many, A., Goldstein, Y., and Grover, N. B. 1965, Semiconductor Surfaces, Noth-Holland Publishing Company, Amsterdam,
36. Morrison, S. R. 1953, J. Phys. Chem., 57, 860.
37. Munakata, C., Yagi, K., Warabisako, T., Nanba, M., and Matsubara, S. 1982, Jpn. J. Appl. Phys., 21, 624.
38. Honma, N., Munakata, C., Itoh, H., and Warabisako, T. 1986, Jap. J. Appl. Phys., 25, 743-749.
39. Nakhmanson, S. 1975, Solid State Electron., 18, 617-626.
40. Nakhmanson, S., Ovsyuk, Z. S., and Popov, L. K. 1975, Solid State Electron., 18, 627-634.
41. Park, E., Schroder, D. K., Tan, S. E., Choi, B. D., Fletcher, M., Buczkowski, A., and Kirscht, F. 2001, J. Electrochem. Soc., 148, G411-G419.
42. Ruda, H., and Shik, A. 2002, J. Appl. Phys., 91, 6476-6480.
43. Ryvkin, S. M. 1964, Photoelectric Effects in Semiconductors, Consultants Bureau, New York, 31.
44. Bachrach-Ashkenasy, N., Kronik, L., Shapira, Y., Rosenwaks, Y., Hanna, M. C., Leibovitch, M., and Ram, P. 1996, Appl. Phys. Lett., 68, 879.
45. Ashkenasy, N., Leibovitch, M., Rosenwaks, Y., Shapira, Y., Barnham, K. W. J., Nelson, J., Barnham, K. W. J., and Nelson, J. 1999, JAP, 86, 6902.
46. Ashkenasy, N., Leibovitch, M., Rosenwaks, Y., and Shapira, Y. 2000, Meas. Sci. Eng. B, 74, 125-132.

47. Dumitras, G., and Riechert, H. 2003, J. Appl. Phys., 94, 3955-3959.
48. Datta, S., Ghosh, S., and Arora, B. M. 2001, Rev. Sci. Instr., 72, 177.
49. Huang, Y. S., Malikova, L., Pollak, F. H., Shen, H., Pamulapati, J., and Newman, P. 2000, J. Appl. Phys., 77, 37.
50. Huang, Y. S., Malikova, L., Pollak, F. H., Debray, J.-P., Hoffman, R., Amtout, A., and Stall, R. A. 2002, J. Appl. Phys., 91, 6203.
51. Liang, J. S., Wang, S. D., Huang, Y. S., Malikova, L., Pollak, F. H., Debray, J. P., Hoffman, R., Amtout, A., and Stall, R. A. 2003, J. Appl. Phys., 93, 1874.
52. Liang, J. S., Huang, Y. S., Tien, C. W., Chang, Y. M., Chen, C. W., Li, N. Y., Li, P. W., and Pollak, F. 2001, Appl. Phys. Lett., 79, 3227.
53. Wang, S. D., Liang, J. S., Huang, Y. S., Tien, C. W., Chang, Y. M., Chen, C. W., Li, N. Y., Tiong, K. K., and Pollak, F. H. 2002, J. Appl. Phys., 92, 2350.
54. Liang, J. S., Wang, S. D., Huang, Y. S., Tien, C. W., Chang, Y. M., Chen, C. W., Li, N. Y., and Pollak, F. H. 2002, Appl. Phys. Lett., 80, 752.
55. Sitarek, P., Hsu, H. P., Huang, Y. S., J. M. Lin, H. H. Lin, and Tiong, K. K. 2009, J. Appl. Phys., 105, 123523.
56. Sharma, T. K., Fox, N. E., Hosea, T. J. C., Nash, G. R., Coomber, S. D., Buckle, L., Emeny, M. T., and Ashley, T. 2008, Appl. Phys. Express, 1, 062001.
57. Chan, C. H., Chen, H. S., Kao, C. W., Hsu, H. P., Huang, Y. S., and Wang, J. S. 2006, Appl. Phys. Lett., 89, 022114.
58. Chan, C. H., Huang, Y. S., Wang, J. S., and Tiong, K. K. 2007, Optics Express, 15, 1898-1906.
59. Simpkins, B. S., Schaadt, D. M., and Yu, E. T. 2002, J. Appl. Phys., 91, 9924.
60. Lin, Y., Wang, D., Zhao, Q., Yang, M., and Zhang, Q. 2004, J. Phys. Chem. B, 108, 3202-3206.
61. Zhao, Q., Wang, D., Peng, L., Lin, Y., Yang, M., and Xie, T. 2007, Chemical Physics Letters, 434, 96-100.
62. Lin, Y., Wang, D., Zhao, Q., Li, Z., Ma, Y., and Yang, M. 2006, Nanotechnology, 17, 2110-2115.
63. Zhao, Q., Yu, M., Xie, T., Peng, L., PingWang, and Wang, D. 2008, Nanotechnology, 19, 245706.
64. Liu, F., Li, X., Zhao, Q., Hou, Y., Quan, X., and Chen, G. 2009, Acta Materialia, 57, 2684-2690.
65. Donchev, V., Germanova, K., Shtinkov, N., and Vlaev, S. J. 2006, Electronic structure and optical properties of AlAs/GaAs superlattices containing embedded GaAs quantum wells with abrupt and graded interfaces, in: Frontal Semiconductor Research, Chang, O. T. (Ed.), Nova Science Publishers, Inc., New York, 25-60.
66. Blood, P. 1991, in: Physics and Technology of Heterojunction Devices, Morgan, D. V., and Williams, R. H. (Eds.), Peter Perigrinus, London, UK, 231-279.
67. Madelung, O. (Ed.) 1991, Data in Science and Technology. Semiconductors: Group IV Elements and III-V Compounds, Springer, Berlin, 1.
68. Herman, M. A., Bimberg, D., and Christen, J. 1991, J. Appl. Phys., 70, R1.
69. Shtinkov, N., Donchev, V., Germanova, K., Vlaev, S., and Ivanov, I. 2000, Vacuum, 58, 561.
70. Kupka, R. K., and Chen, Y. 1995, J. Appl. Phys., 77, 1990.
71. Chomette, A., Lambert, B., Deveaud, B., Clerot, F., Regreny, A., and Bastard, G. 1987, Europhys. Lett., 4, 461.
72. Cavailles, J. A., Miller, D. A., Cunningham, J. E., Wa, P. L. K., and Miller, A. 1992, IEEE J. Quntum Electron., 28, 2486-97.
73. Mendez, E. E., and Bastard, G. 1993, Physics Today, 46, 34-42.
74. Liu, Q., Ruda, H. E., Chen, G. M., and Simard-Normandin, M. 1996, J. Appl. Phys., 79, 7790.
75. Liu, Q., Chen, C., and Ruda, H. 1993, J. Appl. Phys., 74, 7492.
76. Schwertberger, R., Gold, D., Reithmaier, J. P., and Forchel, A. 2003, J. Crystal Growth, 251, 248-252.
77. Alen, B., Martínez-Pastor, J., Garcia-Cristobal, A., González, L., and Garcia, J. M. 2001, Appl. Phys. Lett., 78, 4025-4027.
78. Fuster, D., González, M. U., González, L., González, Y., Ben, T., Ponce, A., Molina, S. I., and Martínez-Pastor, J. 2004, Appl. Phys. Lett., 85, 1424-1426.

79. Sidor, Y., Partoens, B., Peeters, F. M., Ben, T., Ponce, A., Sales, D. L., Molina, S. I., Fuster, D., González, L., and González, Y. 2007, Phys. Rev. B, 75, 125120.
80. Mazur, Y. I., Dorogan, V. G., Bierwagen, O., Tarasov, G. G., DeCuir, J. E. A., Noda, S., Zhuchenko, Z. Y., Manasreh, M. O., Masselink, W. T., and Salamo, G. J. 2009, Nanotechnology, 20, 065401.
81. Dion, C., Desjardins, P., Shtinkov, N., Robertson, M. D., and Schiettekatte, F. 2008, Phys. Rev. B, 77, 075338.
82. Fang, Z. M., Ma, K. Y., Jaw, D. H., Cohen, R. M., and Stringfellow, G. B. 1990, J. Appl. Phys., 67, 7034-7039.
83. Ulloa, J. M., Koenraad, P. M., Fuster, D., González, L., and González, Y. 2008, Nanothecnology, 19, 445601.
84. Fuster, D., González, M. U., González, L., González, Y., Ben, T., Ponce, A., and Molina, S. I. 2004, Appl. Phys. Lett., 84, 4723-4725.
85. Saito, H., Nishi, K., and Sugou, S. 2001, Appl. Phys. Lett., 78, 267.
86. Wang, R. H., Stintz, A., Varangis, P. M., Newell, T. C., Li, H., Malloy, K. J., and Lester, L. F. 2001, IEEE Photonics Technol. Lett., 13, 767.
87. Eliseev, P. G., Li, H., Stintz, A., Liu, G. T., Newel, T. C., Malloy, K. J., and Lester, L. F. 2000, Appl. Phys. Lett., 77, 262.
88. Park, Y. M., Park, Y. J., Kim, K. M., Shin, J. C., Song, J. D., Lee, J. L., and Yoo, K. H. 2004, Phys. Rev. B, 70, 035322.
89. Li, E. H. (Ed.) 1997, Semiconductor Quantum Wells Intermixing: Material Properties and Optoelectronic Applications, Gordon and Breach, The Netherlands.
90. Bhattacharyya, D., Helmy, A. S., Bryce, A. C., Avrutin, E. A., and Marsh, J. H. 2000, J. Appl. Phys., 88, 4619.
91. Djie, H. S., Wang, Y., Negro, D., and Ooi, B. S. 2007, Appl. Phys. Lett., 90, 031101.
92. Wang, Y., Djie, H. S., and Ooi, B. S. 2006, Appl. Phys. Lett., 88, 111110.
93. Djie, H. S., Ooi, B. S., and Aimez, V. 2005, Appl. Phys. Lett., 87, 261102.
94. Djie, H. S., Ooi, B. S., and Gunawan, O. 2006, Appl. Phys. Lett., 89, 081901.
95. Sun, B. Q., Lu, Z. D., Jiang, D. S., Wu, J. Q., Xu, Z. Y., Wang, Y. Q., Wang, J. N., and Ge, W. K. 1998, Appl. Phys. Lett., 73, 2657.
96. Bauer, R. S., and Margaritondo, G. 1987, Physics Today, 40, 26-34.
97. Jansens, K. L., Partoens, B., and Peeters, F. M. 2002, Phys. Rev. B, 66, 075314.
98. Madureira, J. R., Godoy, M. P. F. d., Brasil, M. J. S. P., and Iikawa., F. 2007, Appl. Phys. Lett., 90, 212105.
99. Veloso, A. B., Nakaema, M. K. K., Godoy, M. P. F. d., Lopes, J. M. J., Iikawa, F., Brasil, M. J. S. P., Bortoleto, J. R. R., Cotta, M. A., Fichtner, P. F. P., Morschbacher, M. J., and Madureira, J. R. 2007, App. Phys. Lett., 91, 121917.
100. Gradkowski, K., Ochalski, T. J., Williams, D. P., JunTatebayashi, Khoshakhlagh, A., Balakrishnan, G., O'Reilly, E. P., Huyet, G., Dawson, L. R., and Huffaker, D. L. 2009, J. Luminescence, 129, 456-460.
101. Krenner, H. J., Pryor, C. E., He, J., and Petroff, P. M. 2008, Nano Letters, 8, 1750.
102. Nakaema, M. K. K., Iikawa, F., Brasil, M. J. S. P., Ribeiro, E., Medeiros-Ribeiro, G., Carvalho, W., Maialle, J. M. Z., and Degani, M. H. 2002, Appl. Phys. Lett., 81, 2743.
103. Godoy, M. P. F. d., Gomes, P. F., Nakaema, M. K. K., Iikawa, F., Brasil, M. J. S. P., Caetano, R. A., Madureira, J. R., Bortoleto, J. R. R., Cotta, M. A., Ribeiro, E., Marques, G. E., and Bittencourt, A. C. R. 2006, Phys. Rev. B, 73, 033309.
104. Solomon, G. S., Trezza, J. A., Marshall, A. F., and Harris, J. S. 1996, Phys. Rev. Lett., 76, 952.